A unified framework for earthquake sequences and the growth of geological structure in fold-thrust belts

Rishav Mallick[1], Roland Burgmann[2], Kaj M. Johnson[3], and Judith Hubbard[4]

[1]Earth Observatory of Singapore
[2]University of California, Berkeley
[3]Indiana University Bloomington
[4]Nanyang Technological University

November 24, 2022

Abstract

Observations of fold growth in fold-thrust belt settings show that brittle deformation can be localized or distributed. Localized shear is associated with frictional slip on primary faults, while distributed brittle deformation is recognized in the folding of the bulk medium. The interplay of these processes is clearly seen in fault-bend folds, which are folds cored by a fault with an abrupt change in dip (e.g., a ramp-décollement system). While the kinematics of fault-bend folding were described decades ago, the dynamics of these structures remain poorly understood, especially the evolution of fault slip and off-fault deformation over different periods of the earthquake cycle. In order to investigate the dynamics of fault-bend folding, we develop a numerical modeling framework that combines a long-term elasto-plastic model of folding in a layered medium with a rate-state frictional model of fault strength evolution in order to simulate geologically and mechanically consistent earthquake sequences. In our simulations, slip on the ramp-décollement fault and inelastic fold deformation are mechanically coupled processes that build geologic structure. As a result, we observe that folding of the crust does not occur steadily in time but is modulated by earthquake cycle stresses. We suggest combining seismological and geodetic observations with geological fault models to uncover how elastic and inelastic crustal deformation generate fault-bend folds. We find that distinguishing between the elastic and inelastic response of the crust to fault slip is possible only in the postseismic period following large earthquakes, indicating that for most fault systems this information currently remains inaccessible.

A unified framework for earthquake sequences and the growth of geological structure in fold-thrust belts

Rishav Mallick[1,2,*], Roland Bürgmann[3], Kaj Johnson[4] and Judith Hubbard[1,2]

[1]Asian School of the Environment, Nanyang Technological University, Singapore
[2]Earth Observatory of Singapore, Nanyang Technological University, Singapore
[3]University of California, Berkeley, USA
[4]Indiana University at Bloomington, USA

[*]Corresponding author: Rishav Mallick (rishav001@e.ntu.edu.sg)

Main points

1. Bends in thrust faults create unbalanced elastic stresses within the surrounding medium, which must be relaxed by off-fault deformation (OFD).
2. We couple an elasto-plastic boundary element model with a frictional boundary integral framework to generate geologically-consistent earthquake sequences.
3. We discuss strategies to observe OFD processes using combined seismo-geodetic methods, noting that the postseismic period may be the most appropriate observational period.

Abstract

Observations of fold growth in fold-thrust belt settings show that brittle deformation can be localized or distributed. Localized shear is associated with frictional slip on primary faults, while distributed brittle deformation is recognized in the folding of the bulk medium. The interplay of these processes is clearly seen in fault-bend folds, which are folds cored by a fault with an abrupt change in dip (e.g., a ramp-décollement system). While the kinematics of fault-bend folding were described decades ago (J. Suppe, 1983), the dynamics of these structures remain poorly understood, especially the evolution of fault slip and off-fault deformation over different periods of the earthquake cycle. In order to investigate the dynamics of fault-bend folding, we develop a numerical modeling framework that combines a long-term elasto-plastic model of folding in a layered medium with a rate-state frictional model of fault strength evolution in order to simulate geologically and mechanically consistent earthquake sequences. In our simulations, slip on the ramp-décollement fault and inelastic fold deformation are mechanically coupled processes that build geologic structure. As a result, we observe that folding of the crust (like fault slip) does not occur steadily in time but is modulated by earthquake cycle stresses. We suggest combining seismological and geodetic observations with geological fault models to uncover how elastic and inelastic crustal deformation generate fault-bend folds. We find that distinguishing between the elastic and inelastic response of the crust to fault slip is possible only in the postseismic period following large earthquakes, indicating that for most fault systems this information currently remains inaccessible.

1. Introduction

Geophysical models often assume that the lithosphere is broken into elastic blocks along plate boundary faults, and all inelastic (permanent) deformation is focused within the fault zone (Reid, 1911). This simplification is typically applied to interpret short-term observations related to the earthquake cycle. For example, many fault models are composed of a dislocation plane inserted into an elastic medium, with geodetic and seismological observations interpreted as the response of the medium to localized shear (slip) on the fault (e.g., Kanda & Simons, 2010; Okada, 1985; Savage, 1983; Singh & Rani, 1993). The success of this computationally inexpensive approach in matching observations relative to the data uncertainty has reinforced its use (Savage, 1983; Vergne et al., 2001; Van Zwieten et al., 2013).

However, this description of tectonics is unable to reproduce a fundamental observable: the ability of fault slip to permanently deform the lithosphere and generate relief. While planar dislocations may sufficiently approximate faults over some timescales, additional considerations must be incorporated into tectonic models in order to bridge timescales (from the seconds to years of geodetic and seismic data, to the tens of thousands to millions of years associated with mountain building) and develop geologically consistent representations of crustal deformation.

1.1. Fault bends and unbalanced stress

The issue of crustal deformation is particularly relevant in convergent margins, where shortening of the crust is accommodated along thrusts with associated folding. In these settings, a gently dipping subduction megathrust or continental thrust separates the down-going plate from the overriding plate (Figure 1a). Typically, the hanging wall of the megathrust will host a series of more steeply dipping splay faults or ramps, with the younger thrusts near the toe of the system. When shortening is accommodated across this system, slip on the megathrust will be transferred onto one of the steeper splays, resulting in an active fault bend (Figure 1).

77

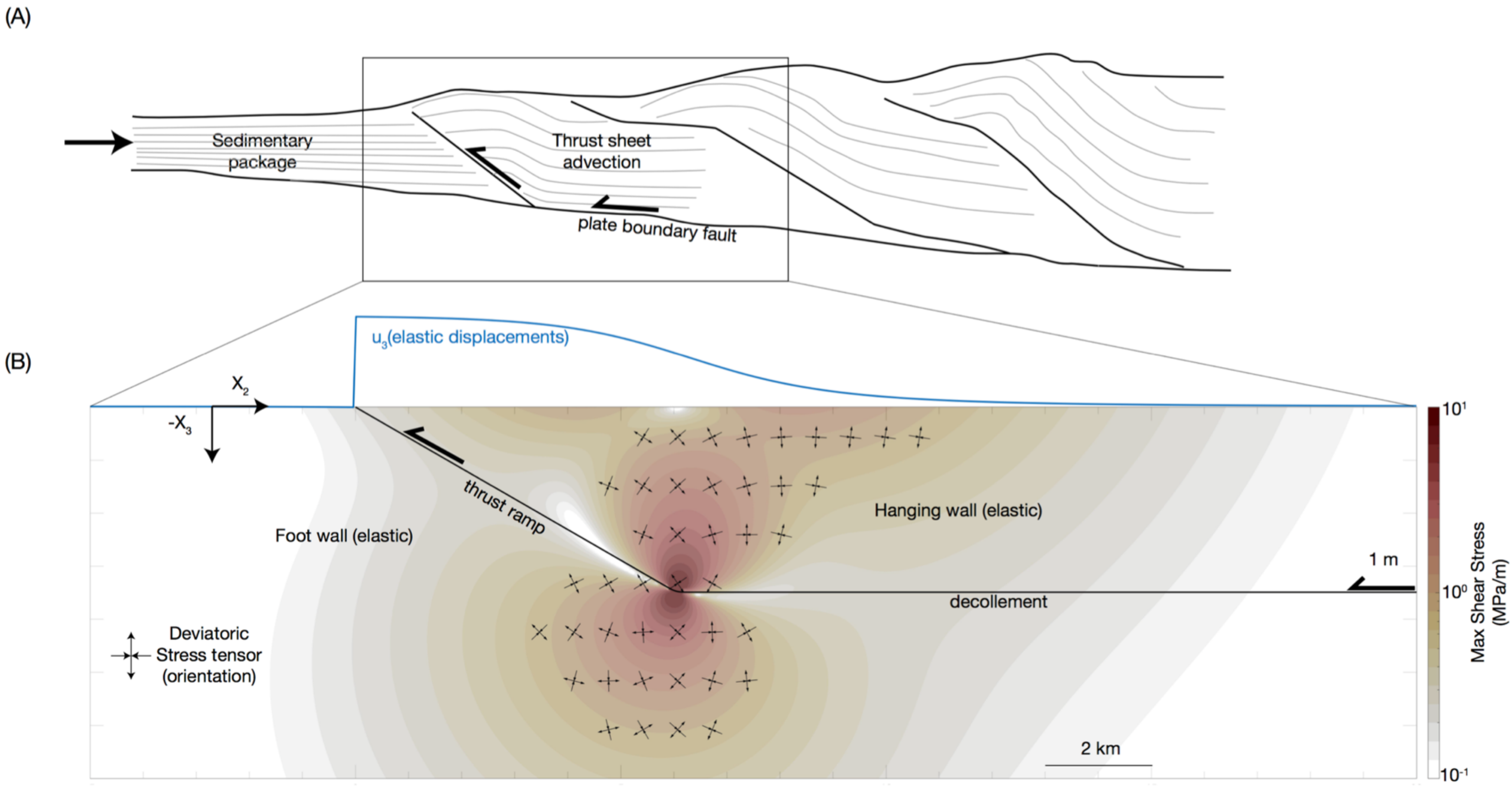

Figure 1. Shear stress inside an elastic medium grows with slip on a non-planar fault. (A) Schematic of a fold-thrust belt. Shortening causes faulting and folding of the initially horizontal the sedimentary package. (B) Model of the frontal fault and fold. For 1 m of slip on the ramp-décollement system, the surface uplift due to a purely elastic response of the crust is shown in blue. Background colors show maximum shear; black crosses show the orientation of the deviatoric part of the stress tensor (inward arrows - compression, outward arrows - extension).

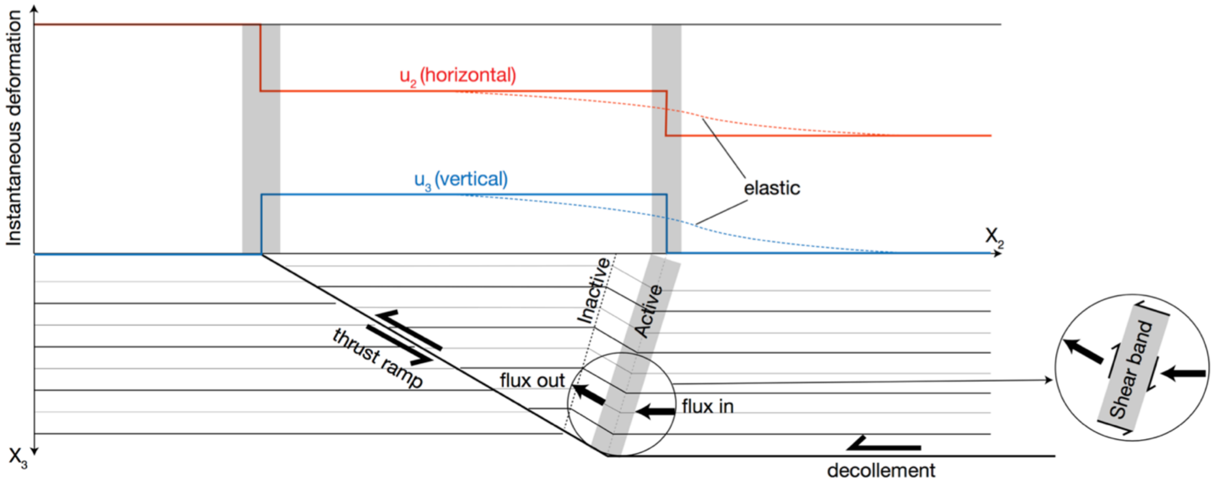

Figure 2. Surface deformation due to fault-bend folding. Fault slip leads to the formation of an axial surface/hinge within the hanging wall, at the junction of the ramp and décollement. This hinge is a shear band that is stationary with respect to the ramp and décollement and does not advect with the thrust sheet (shown by the flux of material passing through the hinge). The horizontal (red) and vertical (blue) instantaneous displacement fields are shown in response to unit slip (assuming infinitesimal strains) for fault-bend folding (solid) and elastic (dashed) deformation. The displacement gradients are sharp across the hinge as we assume that the fault bend is infinitesimally narrow, and hence the shear band appears as a backthrust.

In most modeling studies of crustal deformation based on seismological and geodetic data, both the footwall and the hanging wall are assumed to behave as linear elastic solids over short timescales (seconds – years). Such an assumption is appropriate for planar faults, where uniform slip on the interface results in a net translation between the hanging wall and footwall. However, slip across a geometric bend leads to unbalanced shear stresses within an elastic medium (Figure 1b). These stress components grow with accrued slip on the main fault, and cannot be supported indefinitely by a purely elastic body. In order to generate an internally consistent modeling approach, some mechanism(s) must be added to relax these stresses. Ideally, the mechanisms that are added will also produce structures consistent with geological observations of fault bends in fold-thrust environments (Figure 2). By implementing geologically consistent mechanisms into elastic dislocation modeling approaches, we can therefore solve two problems at once: (1) balance shear stress loads due to slip on non-planar faults, and (2) create permanent crustal deformation and build relief.

1.2.Off-fault deformation

In order to relax unbalanced stresses within the crust, inelastic deformation must occur away from the main fault i.e. off-fault deformation (OFD). Geological observations of anticlines in fold-thrust belts show that permanent OFD occurs through inelastic shear, and can manifest in various ways (Butler et al., 2020; Cosgrove, 2015; Shaw et al., 1999; J. Suppe, 1983; John Suppe et al., 2005). These include localized slip on a backthrust (conjugate to the main thrust) to create a pop-up structure (Gregg Erickson et al., 2005), slip on bedding plane contacts within the fold (A. M. Johnson & Berger, 1989; J. Suppe, 1983), layer buckling and viscous/plastic flow of weak layers (Berger & Johnson, 1980; Biot, 1964; Butler et al., 2020; Fletcher, 1977; Honea & Johnson, 1976; H. Ramberg, 1963, 1970), and distributed deformation by thickening/thinning of individual layers within a thrust sheet (Honea & Johnson, 1976; A. M. Johnson & Pfaff, 1989; Poblet & McClay, 1996). In this article, we specifically address folding of the hanging wall accommodated by bedding plane slip (which is equivalent to layer buckling); this mechanism relaxes the unbalanced elastic stresses in the hanging wall that arise from slip on the ramp-décollement system.

1.3.Fault-bend folding and displacement fields

The kinematic theories of fault-bend folding and buckle folding describe the growth of a fault-cored fold by bedding plane slip within an incompressible hanging wall (Brandes & Tanner, 2014; A. M. Johnson & Berger, 1989; J. Suppe, 1983; John Suppe et al., 2005). Since bedding plane thickness is typically conserved as a thrust sheet is advected through a fault bend, the amount of slip on the fault and the shape of the resulting fold are directly linked (J. Suppe, 1983)

For example, consider a ramp-décollement system with initial horizontal layering (Figure 2). As the thrust sheet is advected through the fault bend, a shear band appears in the hanging wall; this is the active axial surface or the hinge zone. If fault bend occurs over infinitesimal width, then the axial surface will be infinitesimally narrow, and the instantaneous surface displacement field will be identical to that above a backthrust (Figure 2).

However, axial surfaces and backthrusts are fundamentally different in their long-term kinematics (Gregg Erickson et al., 2005; Gregg Erickson & Jamison, 1995; J. Suppe, 1983). While a backthrust will be progressively advected up the main thrust ramp, an active axial surface is fixed relative to the underlying fault geometry. The active axial surface is paired with an inactive axial surface; the latter represents the initial lower limit of the hanging wall above the fault bend that has been advected up the ramp. The spatial separation of the inactive and active axial surfaces therefore represents the slip on the fault ramp after finite shortening. Although the geometries of the two axial surfaces appear similar, active deformation occurs only at the active axial surface (Figure 2).

The deformation in the hinge zone (active axial surface) can be considered to represent either slip on the bedding plane contacts or focused viscous/plastic shear of thin mechanically weak beds (while thicker and stronger beds remain undeformed). This type of deformation occurs because the transverse anisotropy in a stack of sediments allows mechanically stronger beds to retain their shape and structure, with shear localizing either within weaker beds or along the interfaces between beds (Figure 2). Most numerical models of fault-related deformation neglect this type of deformation because it requires knowledge of the orientations of the bedding planes in the hanging wall, information that is typically difficult to access, and in the case of imbricated fold-thrust belts, may be complex.

The net surface displacement field associated with this mechanism has large displacement gradients at two locations (Figure 2): (1) where the thrust ramp intersects with or comes closest to the free surface, and (2) where the active axial surface intersects the free surface. A model that represents only the elastic response of the medium to slip on a ramp-décollement system cannot reproduce the second displacement gradient at the back of the fold (Figure 1b, 2). This implies that there is diagnostic power in looking for such hinge-related OFD signals in geodetic displacement fields over growing folds, in order to study how the crust deforms in response to fault slip and infer its constitutive properties.

1.4.Geodetic observations of fault-bend folding

While geological mapping and sub-surface imaging provide information about the long-term growth of anticlines (integrated over multiple earthquake sequences), geodetically derived deformation fields are sensitive to the earthquake cycle and contain information regarding the time-varying nature of deformation (Allmendinger et al., 2009). It is therefore somewhat surprising that geodetic observations of convergent margins over the interseismic period show a pronounced uplift zone in the same location as uplift recorded in geological and geomorphological proxies representing millions of years (Grandin et al., 2012; Jackson & Bilham, 1994; Meade, 2010; Saillard et al., 2017). These observations, along with the common assumption that folding occurs as a viscous process (Biot, 1961; H. Ramberg, 1970; I. B. Ramberg & Johnson, 1976), has led to speculation that the growth of geological structure may be a time-invariant process occurring mostly during the slow and long-lived interseismic period, at rates below the detectability limit (Jolivet et al., 2020; Meade, 2010; Saillard et al., 2017).

However, observations of earthquakes demonstrate that inelastic hanging wall deformation can occur during the coseismic and postseismic phases of the earthquake cycle (Figure 3). The coseismic displacement field from the 1991 M_w 7.6 Chi-Chi earthquake, Taiwan (data from Kuo et al., 2014), shows meter-scale displacements associated with OFD (Figure 3a-b) that produced a meter-scale coseismic fold scarp (Chen et al., 2007). Furthermore, time varying growth of the Kurit fold in Iran documents likely postseismic OFD. These observations, based on ~20 years of InSAR line-of-sight displacement fields (Figure 3c-d), show a signal on the order of 1-5 mm/yr, decaying with time; the signal is presumably a response to an initial stress perturbation caused by the 1978 M_w 7.3 Tabas-e-Golshan earthquake (data from Zhou et al., 2018; Copley, 2014). The coseismic displacement field for the Chi-Chi earthquake and the postseismic velocity field over the Kurit fold both show two large spatial gradients, similar to the prediction for axial surface deformation (Figure 2); we interpret this to be the result of fault-bend folding above a ramp-décollement system. These observations demonstrate that inelastic deformation, likely associated with bedding plane slip, occurs over a finite length scale, is a time-varying process, and can be modulated by the earthquake cycle.

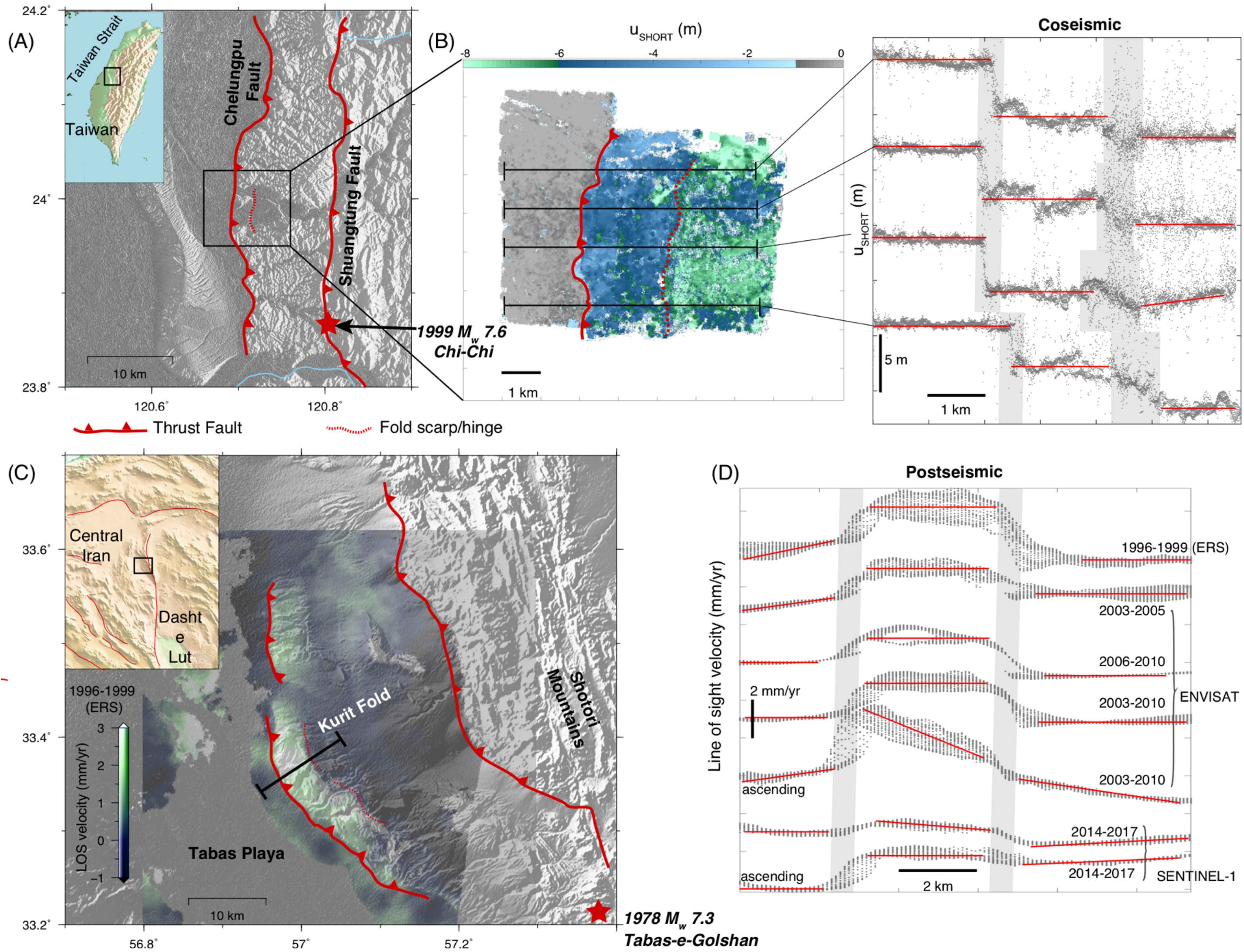

Figure 3. Observations of fault-bend folding modulated by the earthquake cycle. (A) The frontal rupture of the Chelungpu Fault in the 1999 M_w7.6 Chi-Chi earthquake, western Taiwan. (B) Horizontal coseismic displacement field (Kuo et al., 2014) from optical imagery. We highlight four transects exhibiting significant displacement gradients likely due to hinge deformation, as predicted in Figure 2. (C) Postseismic deformation, average velocity field from 1996-1999, of the frontal folds of the Tabas foldbelt following the 1978 M_w7.3 Tabas-e-Golshan earthquake. (D) Shallow fold growth (Kurit fold) has been imaged in the line-of-sight direction (mostly vertical) from 1996-2017 by multiple InSAR missions (Zhou et al., 2018; Copley et al., 2014). The data are acquired in descending mode unless explicitly specified. We observe temporally decaying deformation with a significant displacement gradient in the back limb of the fold, likely caused by hinge deformation.

To understand how brittle faulting and folding can occur simultaneously, we develop a framework to incorporate bedding-plane slip at earthquake timescales, by estimating the down-dip width (length-scale) of the actively deforming hinge zone, and incorporating hinge-related OFD into earthquake sequence simulations and related inverse problems.

We first use a Boundary Element Method (BEM) framework to model a ramp-décollement system in an elasto-plastic medium, incorporating the anisotropy of sedimentary layers (Huang & Johnson, 2016; K. M. Johnson, 2018). We impose shortening in the model and calculate the evolution of geometry and strain-rate within the hanging wall. This model replicates the long-term kinematics of a fault-bend fold while maintaining the stresses in the fault and bedding plane system within the plastic yield envelope. Since hinge deformation in natural ramp-décollement systems has been observed both co- and post-seismically (Figure 3), we take our study a step further to assess how hinge deformation might appear in typical surface observations over timescales associated with seismo-geodetic methods. We do this by calculating the shear stress change from incremental deformation in the elasto-plastic models, and using it to drive earthquake sequence simulations; this computed shear stressing rate serves as the long-term loading rate for the fault and the inelastic regions within the hanging wall. With this loading rate for the fault and hanging wall system, and using the laboratory-derived rate-state friction law to describe the evolution of fault strength (Dieterich, 1979; J. R. Rice & Ruina, 1983; Ruina, 1983), we show that it is now possible to evaluate geologically-consistent earthquake sequence scenarios. The model recreates all parts of the earthquake cycle, from slow interseismic loading to the nucleation of frictional instabilities and an eventual earthquake, as well as the associated OFD in the hinge zone. We discuss the impact of hinge deformation on kinematic inversions of inelastic strain (slip on faults) based on geophysical data from different parts of the earthquake cycle, and evaluate our ability to detect hinge-related OFD using typical seismo-geodetic methods.

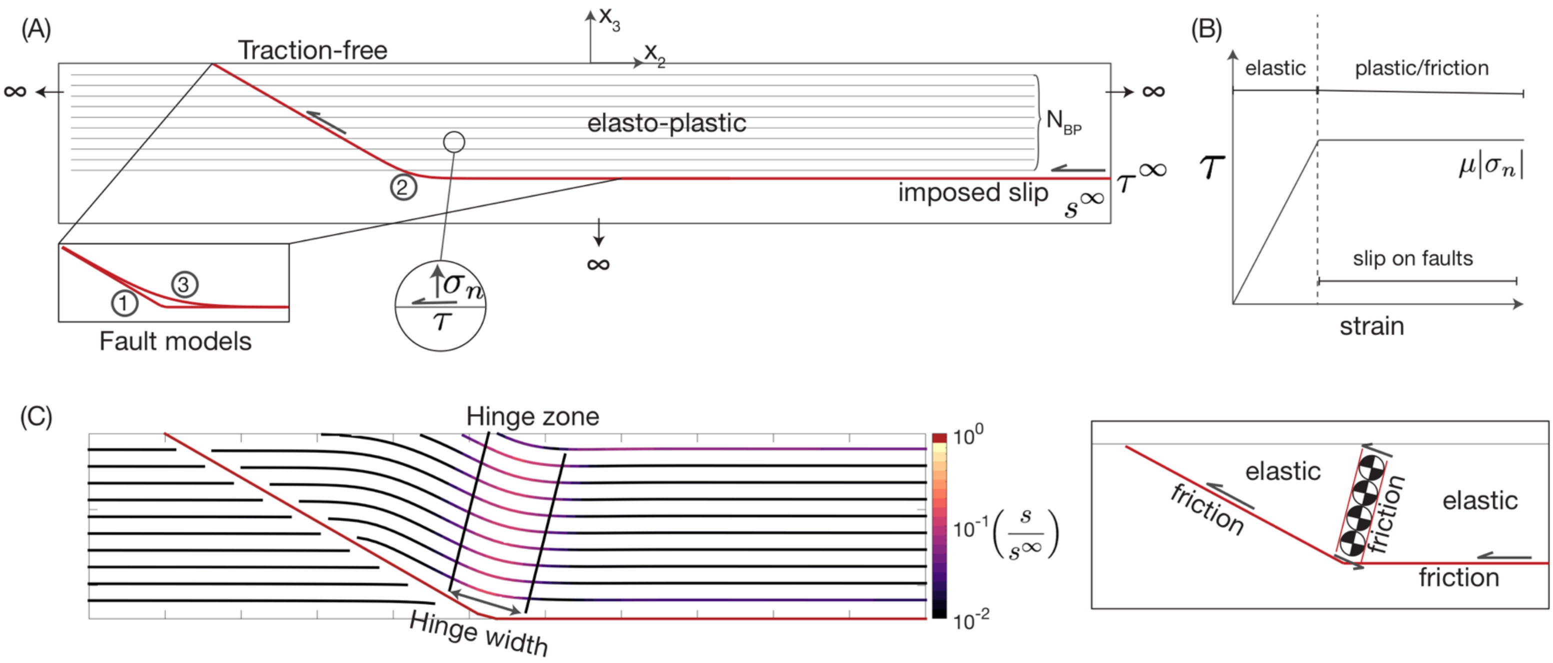

Figure 4. (A) Initial geometry for the elasto-plastic folding models. Slip is imposed on the ramp and décollement as a slip boundary condition; far-field loading is simulated by extending the décollement horizontally for 1000 km (outside the model domain). We consider three different levels of smoothness of the fault bend (1, 2, 3). (B) Elastic-plastic schematic. The medium acts as an elastic body until the yield condition is reached, beyond which inelastic strain is accommodated by slip on the bedding planes shown in (A). (C) The hinge zone is the region within the hanging wall where inelastic deformation occurs (shown in lighter colours, representing more slip on the bedding planes), while the rest of the hanging wall behaves purely elastically (black - no slip). The outputs from the folding model allow us to explicitly define the inelastically deforming domain by its geometry and effective loading rate. In the schematic, we show bedding plane deformation in the hanging wall using double couples to indicate that a series of bedding plane contacts line up to appear as an equivalent thrust fault, in line with our expectations from fault-bend folding (see Figure 2).

2. Methods

We study the effect of maintaining a stress balance/equilibrium over the scale of a single fault-bend fold (Figure 4a). Specifically, we are interested in structures that form close to the free surface, where slip on a décollement is fed onto a ramp; they are therefore thought to be governed by brittle mechanics (Dahlen, 1990). Since we are interested in the combined effects of elastic stress transfer and structural evolution of the system, we are working within a timescale ranging from seconds to 10^6 years. Beyond this timescale, the nucleation and the growth of new faults cannot be neglected, and other mechanisms of deformation and stress redistribution associated with significant changes in geometry occur (Avouac, 2015). Thus, our approach evaluates the short-to-intermediate timescale evolution of the system. At the earthquake cycle timescale, the geometry of the system is essentially static, while at the fold-evolution timescale, we consider the deformation of the hanging wall but ignore both the creation of new faults and any weakening or re-strengthening effects of frictional sliding (Figure 4b).

2.1. Elasto-plastic model of fold growth

We develop a boundary element framework (BEM) following Johnson (2018), in order to investigate how bedding plane slip away from a primary fault can accommodate the development of a fold. Unlike a typical continuum model, we do not evaluate the stress field at every point within the medium. Instead, we assume that bedding planes act as frictional contacts or narrow shear zones, and mesh these bedding contacts using 1-d fault segments (Figure 4a). This reduces the computational expense by exploiting the anisotropy inherent to a stack of sedimentary layers. In our model, initially horizontal strata can deform by passive translation or rotation, as well as by slip on the bedding plane contacts.

We prescribe the rheology of the bedding plane contacts to be elastic-perfectly plastic, governed by Mohr-Coulomb elasto-plasticity (Figure 4b). Specifically, we use the Mohr-Coulomb criterion to model brittle failure (not temperature-dependent plastic flow or ductile creep), governed by a yield condition (Figure 4b) as follows:

$$|\tau^{\infty} + \tau| \leq \mu\bar{\sigma} \qquad 1.$$

Here, τ^{∞} is the remote load (in the shear direction; see Figure 4a) applied to the system. This load can arise from kinematically imposed horizontal shortening across the entire system, topographic loading, or slip on the décollement. In our model, uniform slip on the ramp-décollement fault is imposed as a boundary condition, which loads the hanging wall material. τ is the elastic shear stress field resulting from an arbitrary distribution of slip on the bedding plane contacts. The right-hand side of Equation 1 represents the brittle yield condition: μ is the coefficient of friction on each boundary element, while $\bar{\sigma}$ is the normal stress (normal to the boundary element). This implies that the yield condition on every boundary element is prescribed as a function of normal stress, and the elastic stress within the medium (due to loading) cannot exceed this yield condition. Once it does, the boundary elements will deform by frictional slip to ensure that the residual stress field is within the yield envelope (Figure 4b). In addition to the stress evolution due to slip on various structures, we also consider finite deformation of the medium due to the advection of material and rotation of the bedding plane contacts (Figure 5). This is done by calculating incremental displacements of all boundary elements and remeshing (Johnson, 2018). This change in geometry also modifies the stress field, since the shear stresses resolve differently for different fault and bedding plane dips.

We assume that slip on faults does not change the elastic stress field in the fault-normal direction ($\Delta\bar{\sigma} = 0$). This is primarily to simplify the computations, as including $\Delta\bar{\sigma}$ would make the system of equations difficult to solve with our methodology (discussed later in this section). However, it also allows for the possibility that inelastic perturbations in the fault-normal stress component (deviations from the lithostatic condition) may not persist over long timescales, and are accommodated by other physico-chemical means, such as tensile cracking, fluid flow, pressure solution, and vein formation (Gratier et al., 1999, 2013; Otsubo et al., 2020; Sibson, 2019).

Assuming linear elasticity, we describe the change in elastic shear stress, $\Delta\tau$, arising from incremental slip Δs on the boundary elements as a linear operation (Segall, 2010; Singh & Rani, 1993), given a traction kernel K_τ:

$$\Delta\tau = K_\tau \Delta s \qquad 2.$$

Applying Equation 2 in the failure criterion (Equation 1) gives the condition that must at all times be satisfied for all boundary elements. Because time is absorbed into increments of far-field loading, we write the evolution of slip on the boundary elements as a response to incremental loading, $\Delta\tau^\infty$, as follows,

$$|\tau^\infty + K_\tau s_0| \leq \mu\bar{\sigma} \text{ at } t_0 \qquad 3.$$

$$|\tau^\infty + \Delta\tau^\infty + K_\tau(s_0 + \Delta s)| \leq \mu\bar{\sigma} \text{ at } t_{0^+} \qquad 4.$$

If we define $\tau_+ = \tau^\infty + \Delta\tau^\infty + K_\tau s_0$ in Equation 4, as the instantaneous unbalanced elastic stress field at a given time, the solution for Δs can be formulated as a convex optimization problem. This linearity in the system, despite the use of absolute values, appears because we do not consider changes in the fault-normal stress (as mentioned previously), and can instead use the sign of τ_+ to decompose the solution space of Δs.

$$\begin{array}{ll} \tau_+ > 0 & \begin{array}{c} K_\tau \Delta s \leq \mu\bar{\sigma} - \tau_+ \\ \tau_+ + K_\tau \Delta s \geq 0 \end{array} \\ \\ \tau_+ \leq 0 & \begin{array}{c} -K_\tau \Delta s \leq \mu\bar{\sigma} + \tau_+ \\ \tau_+ + K_\tau \Delta s \leq 0 \end{array} \end{array} \quad 5.$$

$$\text{minimization} \rightarrow \Delta s \sim 0 \quad 6.$$

The set of equations derived from the failure criterion (Equation 5) act as a bounding function for the solution Δs. To uniquely solve for Δs, we apply a least-squares minimization on the incremental slip (Equation 6), since we assume that the physical system wants to do minimal irreversible work to satisfy the stress budget (Equation 1). We use the MATLAB function '*lsqlin*' to do the convex optimization.

Given this framework, we conduct 14 numerical experiments (with varying numbers of bedding layer contact surfaces - Table 1) for three fault geometries (with different degrees of curvature at the fault bend) (Figure 4a). The underlying fault geometry consists of a 5 km long, 30º ramp splaying upward from a horizontal décollement, and is motivated by the observed length scales shown in Figure 3. We are interested in how the width of the hinge zone (*hinge width,* Figure 4c) is affected by both the sharpness of the fault bend and the number of bedding planes (equivalent to the thickness of the bedding layers), since this will be directly relevant in discretizing the domain of inelastic deformation for the earthquake-sequence simulations (section 2.2). In our simulations, we measure the hinge width by fitting the slip distribution on each bedding layer to a Gaussian distribution and finding the 95% confidence interval of the associated shape function.

Table 1: Input parameters for the elasto-plastic fold evolution models	
Number of bedding planes (N_{BP})	5-18
Total shortening (km)	2
Number of slip increments	40
Remote loading slip increments, Δs^{∞}(m)	50
Shear Modulus, G (GPa)	10, 30
Friction coefficient, μ	0.01, 0.1
Poisson's ratio, ν	0.25

2.2.Earthquake sequence simulations

In order to evaluate the impact of hinge-related OFD on earthquake cycle deformation, we develop a set of dynamic rupture simulations informed by the geometries and stress states arising from our models of fold growth (section 2.1). At the timescale of earthquakes and the earthquake cycle, we assume that the geometry of the main fault and the surrounding medium is invariant, since each earthquake accommodates meters of slip while the fold is kilometers wide. We use the fault geometry from Figure 4a (number 2) in the earthquake sequence simulations, since it creates reasonably narrow hinge zones (Figure 7c), but is smooth enough that the kink, which violates the principle of interpenetration of an elastic body (Romanet, 2020), does not strongly influence the results. We take the geometry and instantaneous slip rate values from a 15-layer model run (Figure 5a) after 1.5 km of shortening (the hinge width and slip rates have reached steady state – see Figure 6). We only extract the boundary elements with slip rates greater than 1% of the imposed slip on the ramp-décollement (the slip boundary condition), as this helps to reduce the dimensionality of the simulation while still capturing the deforming regions of the model (Figure 5a).

Although our long-term elasto-plastic fold growth model is able to reproduce geologically validated geometries, that model assumes that fault strength is constant in time, which is not realistic (Figure 4b). In fact, faults weaken and heal with loading conditions, and earthquakes occur when a fault weakens faster than it releases stress by slipping (see review by Scholz, 1998).

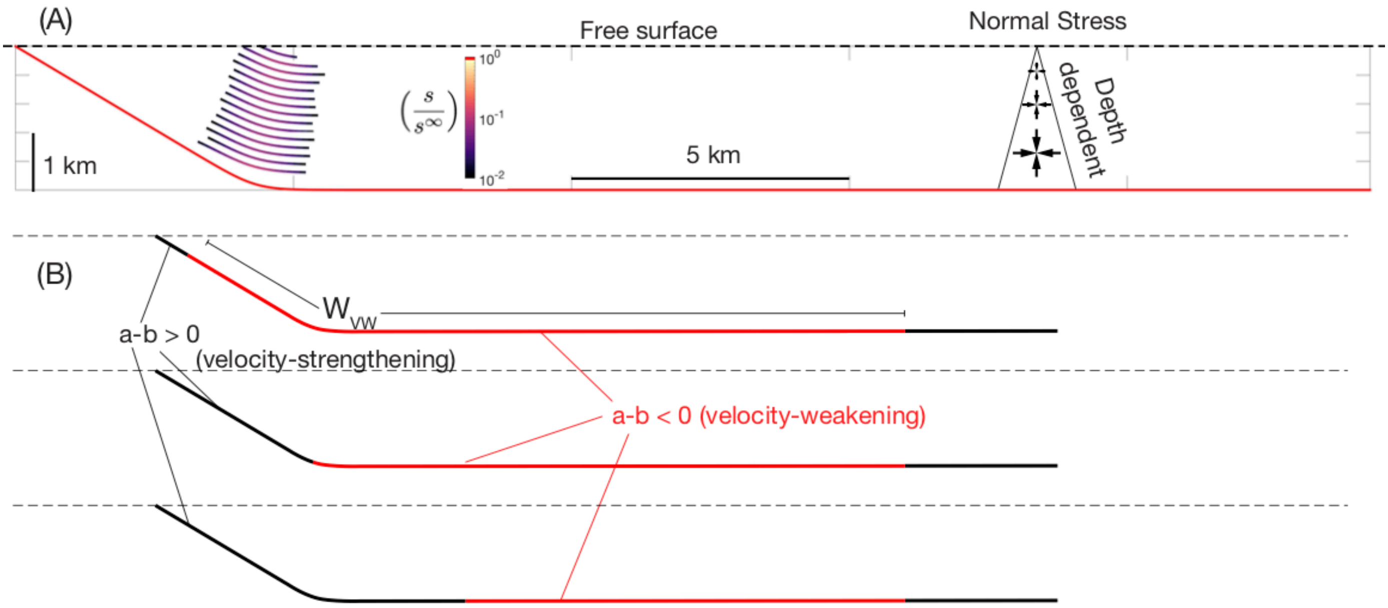

Figure 6. (A) Geometry and model setup for the earthquake sequence simulations (see Table 2 for details). (B) Three scenarios of frictional properties on the fault: red – velocity weakening, black – velocity strengthening.

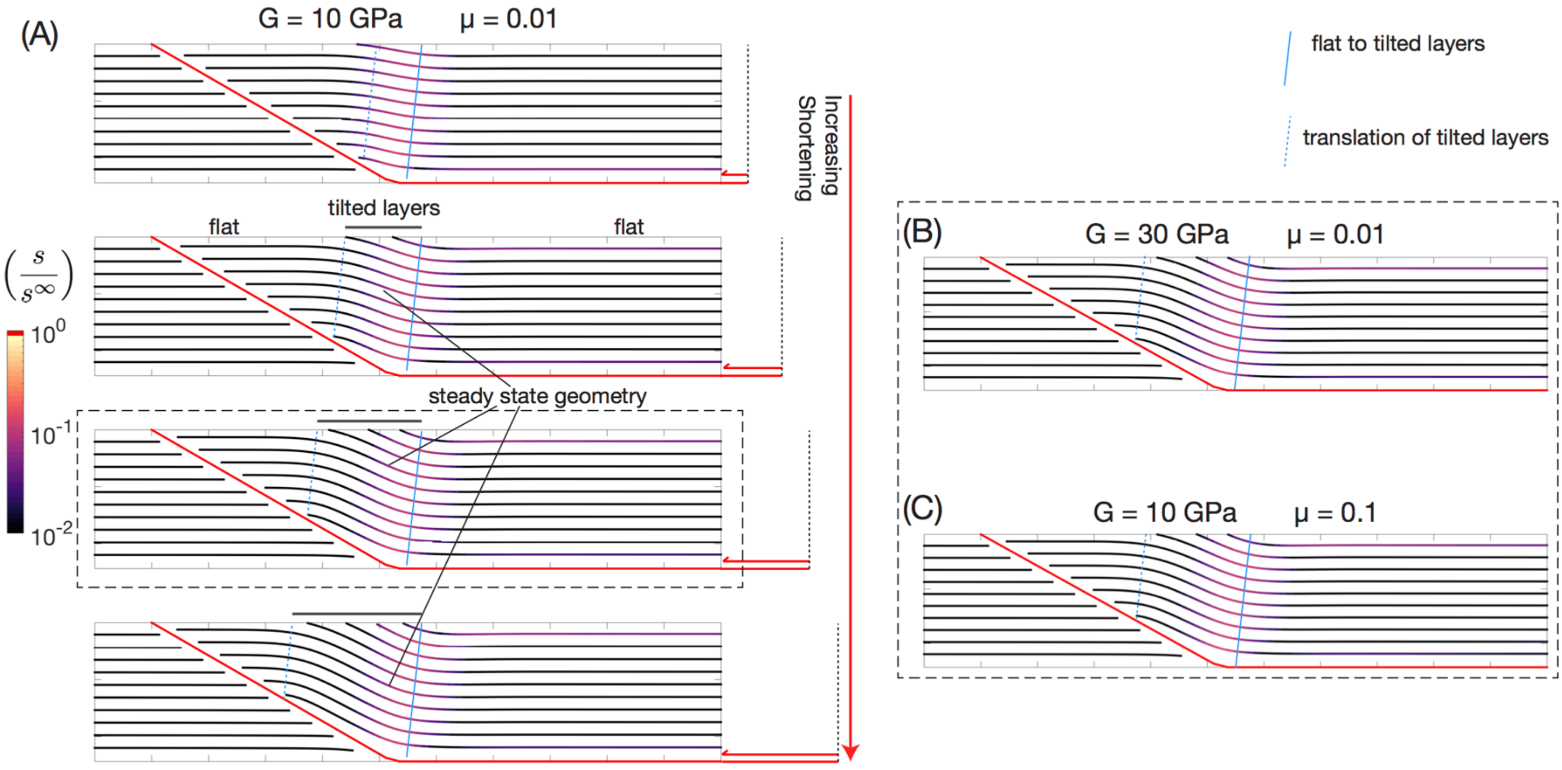

Figure 5. (A) Snapshots of incremental deformation (shown as colored bedding planes) of the hanging wall with increasing shortening. The blue lines approximately separate flat layers from tilted layers. The first snapshot has not yet reached a steady-state geometry; the next three snapshots show steady-state deformation, i.e. the hinge width and slip rate do not vary with incremental deformation. (B) and (C) Equivalent snapshots of simulations with different material properties, compared to the simulation outlined with a dashed box in (A), show that the fold form does not depend on G or μ (layers).

323

Since fold growth with hinge-related OFD has been observed in both co- and post-seismic natural settings, this variation in friction must be considered. In our simulations, we recreate the same cumulative slip and deformation as in the long-term models, while also evaluating the partitioning of slip into the *coseismic*, *postseismic* and *interseismic* phases of the earthquake cycle.

2.2.1. Rate-state frictional earthquake sequences

We treat the boundary elements that make up the ramp-décollement and the hinge zone as elastically coupled faults (Johnson, 2018). These elements are loaded at a known long-term rate, $\dot{\tau}^{\infty} = -K_{\tau}\dot{s}^{\infty}$ (Figure 5a). We derive $\dot{s}^{\infty}$ from the outputs of the long-term simulation. The elasto-plastic long-term simulations have no explicit time dependence since incremental slip drives the system. In order to incorporate time into stress evolution over the earthquake cycle, we need to make a choice for the average slip rate of the system (10^{-9} m/s). The relative variation in Δs can be used to modify $\dot{s}^{\infty}$ accordingly, giving $\begin{bmatrix} \dot{\tau}^{\infty} \\ \dot{\tau}_{OFD}{}^{\infty} \end{bmatrix}$. We use a boundary integral formulation such that the linear momentum balance on these elements is satisfied as the simulation evolves as,

$$\begin{bmatrix} \dot{\tau}^{\infty} \\ \dot{\tau}_{OFD}{}^{\infty} \end{bmatrix} + K_{\tau} \begin{bmatrix} v \\ v_{OFD} \end{bmatrix} = \dot{\mu}\bar{\sigma} + \frac{G}{2v_s} \begin{bmatrix} \dot{v} \\ \dot{v}_{OFD} \end{bmatrix} \qquad 7.$$

The left side of Equation 7 is the instantaneous elastic stressing rate as a function of slip velocity v (resolved in the shear direction for each boundary element). This is a quasi-dynamic approach where we neglect wave-mediated stress transfer through an elastic medium. The right side contains two terms: the first is the rate of change of the frictional strength of each element, and the second the radiation damping rate (a proxy for the energy lost to the system, at velocities comparable to the shear wave velocity v_s). We use rate-state friction and the ageing law to describe the evolution of fault strength with velocity v and a state parameter θ over a critical slip distance L (Dieterich, 1979; Ruina, 1983),

$$\begin{gathered} \mu = \mu_0 + a\log\frac{v}{v_0} + b\log\frac{v_0\theta}{L} \\ \frac{d\theta}{dt} = 1 - \frac{v\theta}{L} \end{gathered} \qquad 8.$$

where μ_0, v_0 are reference values of the friction coefficient and velocity, respectively, while a, b are material-specific constants. Equations 7 and 8 represent a coupled system of ordinary differential equations in v, θ that we solve using the Runge-Kutta 4[th] order adaptive time-stepping solver – MATLAB based *ode45*.

We choose representative values of a, b and L from typical ranges of laboratory-derived studies (Table 2; also see Blanpied et al., 1995). Fault sections with $a - b < 0$ are considered velocity-weakening (i.e. a frictional instability could nucleate on it), while $a - b > 0$ represents a frictionally stable section of a fault, where any slip perturbation is damped back to steady-state. $\bar{\sigma}$ follows a depth-dependent lithostatic condition assuming hydrostatic pore-fluid infiltration; we choose a minimum threshold value for $\bar{\sigma}$ to be 20 MPa (equivalent to a depth of ~1 km) to stabilize the response of the fault close to the free surface. We do not allow $\bar{\sigma}$ for any element to change with slip even though elastic stress calculations would suggest that $\bar{\sigma}$ for boundary elements close to the fault-bend is altered by fault slip. This earthquake-sequence implementation of normal-stress change is a known issue but does not have a physically reasonable and computationally convenient fix as yet. The issue arises because the amplitude of normal stress perturbations are a geometric effect which grow linearly with fault slip (Dunham et al., 2011; Romanet, 2020; Tal et al., 2018); such an issue does not arise in planar fault simulations. Relaxing these stress components may occur through fluid-driven and visco-plastic failure processes (Dunham et al., 2011; Gratier et al., 1999, 2013; Otsubo et al., 2020; Sibson, 2019); these are mechanisms that we do not include in this study, and could be considered in future studies.

In our numerical experiments, we fix all material properties (Table 2) and vary only the location of the up-dip transition from velocity-weakening to velocity-strengthening on the ramp-décollement system (Figure 5b), while the hinge region is considered only to be velocity-strengthening (Figure 5). We choose velocity-strengthening friction for the bedding plane faults that make up the hinge for two reasons: (1) this is one of the first earthquake-sequence studies where we explicitly account for inelastic strain associated with off-fault bedding plane slip, and so, do not want to explore too many complicated unknowns simultaneously, and (2) this is a quasi-dynamic simulation, which implies that we may be introducing numerical errors due to neglecting wave effects in the coseismic stress feedback between the fault and the hinge region, an effect which is exacerbated when the hinge can behave in a frictionally unstable manner.

We define the instability ratio, $\frac{W_{VW}}{h^*}$, as the ratio of the width of the velocity-weakening region, W_{VW} (Figure 5b), to a critical nucleation length-scale (Rubin & Ampuero, 2005), defined as,

$$h^* = \frac{GL}{(1-\nu)(b-a)\bar{\sigma}} \qquad 9.$$

The instability ratio is a key parameter that is thought to determine the complexity of earthquake sequences, with low values (1-10) showing quasi-periodic slow-slip and system-wide ruptures, to high values (>100) showing aperiodic Gutenberg-Richter earthquake statistics (Cattania, 2019). In this study, we investigate the instability ratio range of 20-30, which is large enough to produce partial ruptures of the seismogenic region (Cattania, 2019) and is computationally convenient to evaluate. We also choose this range because it produces interseismic signals consistent with those observed in typical convergent margins: low to no interseismic shallow creep updip of locked regions (Almeida et al., 2018), and only a gradual unlocking of otherwise locked regions; locked regions being eroded by deep creep in the years building up to an earthquake induce minimal curvature to the surface displacement timeseries (Bruhat & Segall, 2016; Mavrommatis et al., 2017).

We run three earthquake sequence experiments, for different W_{VW}, on the given fault geometry with hinge-related OFD for a period of 5000 years (Figure 5b); we report the results in the following section.

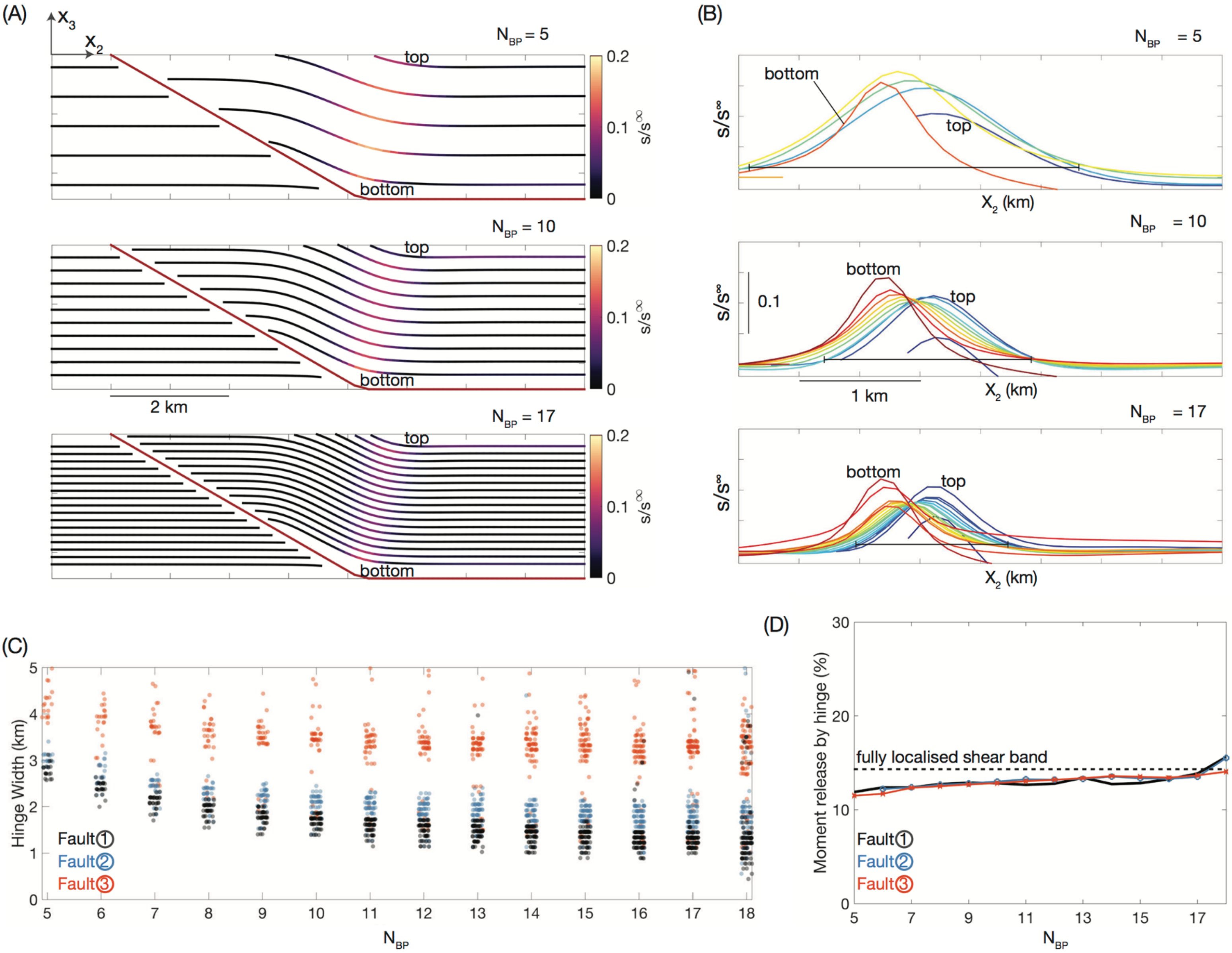

Figure 7. Results of the elasto-plastic folding simulations. (A) Visualization of the length-scale and strain-rate at steady-state for three different experiments associated with Fault 2 (for geometry see Figure 4a). The darker colors of the bedding plane contacts represent no inelastic deformation, while the lighter colors indicate finite slip (normalized by slip imposed on the décollement). The ramp-décollement is marked in red. (B) Slip on each bedding plane is plotted against the horizontal distance X_2. Top and bottom refer to the layers marked in (A). (C) Localization of the hinge (at steady state) is shown as a function of the number of bedding planes (N_{BP}) for the three fault geometries. The estimated hinge width is plotted with some scatter in the x-axis to aid visualization. (D) Comparison between the moment (potency) released by the hinge as a percentage of the total moment released by structures on the order of the length-scale of the fold (~10 km) for each of the fault geometries. Also plotted is the expected moment release by a fully localized shear band based on kinematic fault-bend folding theory.

398

Table 2: Input parameters for earthquake sequence simulations

Property	Value
a	0.01
$a-b$ (velocity weakening)	-0.005
$a-b$ (velocity strengthening)	0.005
v_0 (m/s)	10^{-6}
L (m)	0.01
$\dot{s}^{\infty}$(m/s) plate rate	10^{-9}
Fault dip (º)	Ramp = 30 Décollement = 0
Fault length (km)	Ramp = 5 Décollement = 20
N_{BP}	15
G (GPa)	10
ν	0.25
v_s (m/s)	3000
$\bar{\sigma}$ (MPa), $\rho = 1600\ \mathrm{kg/m^3}$	(Depth-varying) $\rho g X_3$ $\bar{\sigma}_{\min} = 20$
h^* (m)	667
Cohesive Zone (m)	174
Mesh size (m)	50
W_{VW} (km)	13,16,20
Instability Ratio	20,24,30
v_{dyn} (m/s)	0.1

3. Results

In the following sections, we first discuss the length scale associated with the axial surface (hinge width) and the factors that control it, based on our elasto-plastic fold evolution models. We then consider the effects of incorporating hinge-related OFD, using a 15-layer model, into numerical simulations of earthquakes and aseismic processes. We present the results of our elasto-plastic fold evolution models in Figures 6-7, and important results from the earthquake sequence simulations in Figures 8-9.

3.1.Hinge localization

Previous work on multi-layer folding suggests that folding in the brittle crust varies from sinusoidal (large hinge width) to kink bands (narrow hinge width), depending on a combination of material properties – the rigidity of the medium, frictional strength of the layer interfaces, and bed thickness (Biot, 1961, 1964; Honea & Johnson, 1976; Huang & Johnson, 2016; K. M. Johnson, 2018; H. Ramberg, 1970; I. B. Ramberg & Johnson, 1976). In our experiments, we find that the dominant control on hinge width (Figure 7a,b) is instead exerted by the number of bedding planes and the angularity of the primary fault bend (inset Fig. 4a), rather than the shear modulus of the medium, friction coefficient of the bedding plane contacts or the number of slip increments (Figure 6).

This result contrasts with some theoretical studies of buckle folding, which suggest that the final fold form depends on the elastic and frictional properties of the deforming medium (Honea and Johnson, 1976). The discrepancy may be due to the different boundary conditions in our approaches – where Honea and Johnson (1976) considered remote deviatoric loading without any fault, and solved for equilibrium conditions within thin elastic beams, we explicitly drive folding in an elasto-plastic medium with a bent localized slip surface (ramp-décollement fault). In addition, the fault-normal stress in our simulations is depth-dependent pressure and is independent of fault slip. In contrast, fault-cored elasto-plastic simulations that permit the fault-normal stress to change with slip show a dependence on elastic and frictional properties (Johnson, 2018). Specifically, in those models, sharp kink bands tend to form for higher shear strength of the layer interfaces or lower shear modulus of the medium (Johnson, 2018).

Despite the dissimilarities between these approaches and results, in all of the models, the number of bedding planes (equivalent to the bed thickness) exerts a dominant control on folding. Specifically, the hinge narrows as the number of bedding planes increases (Figure 7a,b). Since the number of bedding planes determines the thickness of the bedding layers, increasing the number of bedding planes decreases the bending resistance of the thrust sheet, which may follow the power-law relationship: $\tau_{\mathrm{bending}} \propto \left(\frac{1}{N_{\mathrm{BP}}}\right)^{\alpha}$ (Figure 7c).

This interpretation implies that as $N_{\mathrm{BP}} \to \infty$, the hanging wall will essentially act as a viscous incompressible fluid being transported past a rigid corner (Turcotte and Schubert, 2002). The hinge width in that case will depend entirely on the length scale over which the dip angle changes between the ramp and the décollement. With increasing width of the fault bend (Faults 1-3 in Figure 4a), the hinge width also increases (Figure 7c). At $N_{\mathrm{BP}} = 18$ (the maximum in our model, corresponding to ~100 m thick beds), Fault 3 appears to have reached its asymptotic value, while Fault 1 (kinked fault, see Figure 4a) can likely localize further. We do not explicitly verify the high N_{BP} case, as models with $N_{\mathrm{BP}} > 18$ require increasingly higher resolution of boundary element meshing, which increases the computational cost considerably.

To reinforce the general solution offered by our method, we compare the partitioning of moment between on- and off-fault processes in our models with the kinematics of a fault-bend-fold from velocity vector analysis (A. M. Johnson & Berger, 1989; Sathiakumar et al., 2020). To compute the percentage of moment released by hinge-related OFD, we consider 10 km of the ramp-décollement (consistent with the wavelength of the fold) as the on-fault moment component, while the cumulative moment released by all the individual bedding plane faults is the off-fault component. The values from our simulations match the kinematic results satisfactorily (Figure 7d), indicating that the inelastic component of deformation in our simulations is only a function of the difference in dips of the ramp and décollement. This is consistent with our expectation from the kinematics of fault-bend folding, which depends only on the geometry of the fault and the orientation of the hanging wall rocks (Brandes & Tanner, 2014; A. M. Johnson & Berger, 1989; J. Suppe, 1983).

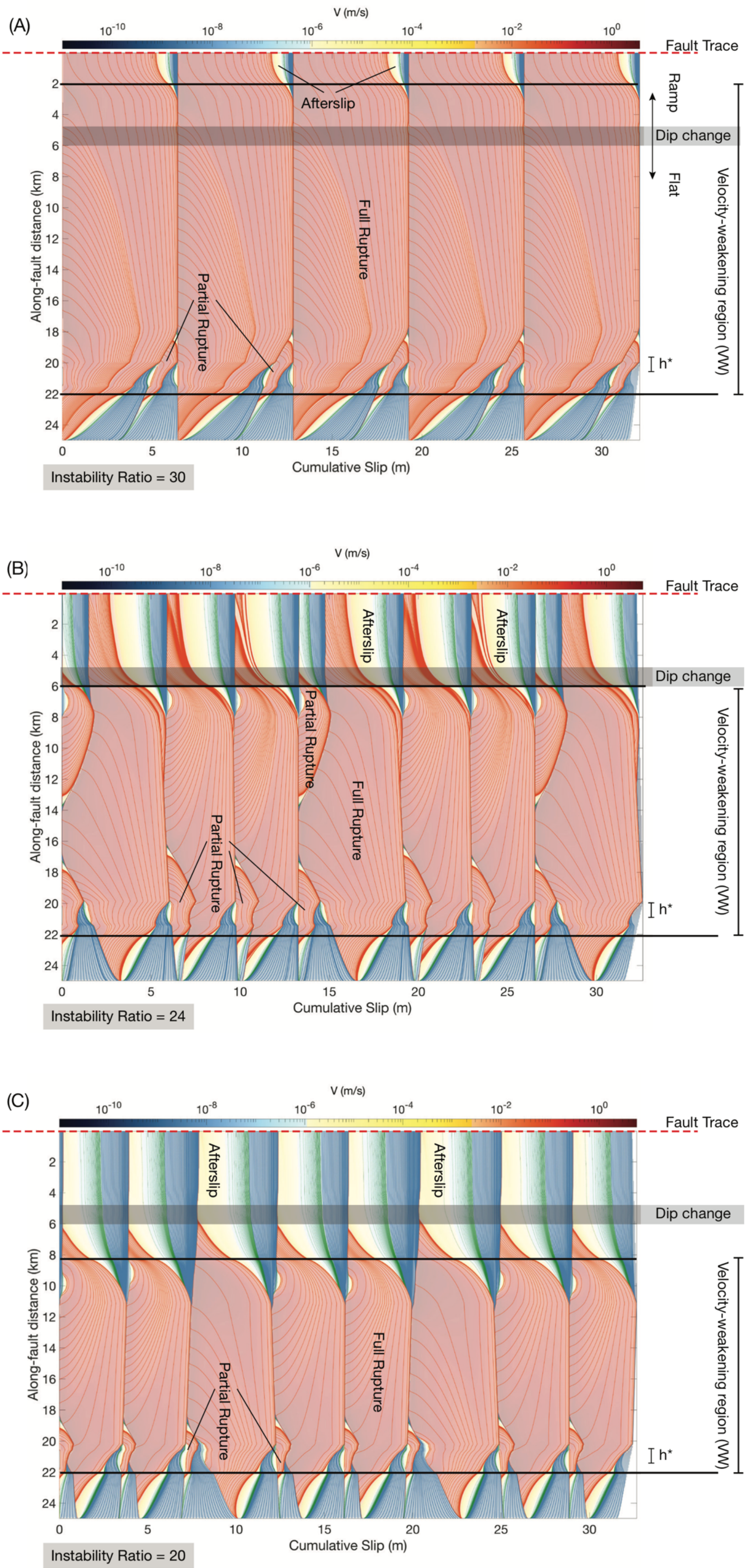
(A)
V (m/s)
Fault Trace
Afterslip
Ramp
Dip change
Flat
Full Rupture
Partial Rupture
Velocity-weakening region (VW)
h*
Along-fault distance (km)
Cumulative Slip (m)
Instability Ratio = 30
(B)
Instability Ratio = 24
(C)
Instability Ratio = 20
(D)
(E)
(F)
Coseismic
Postseismic
VW
VS
Hinge
V (m/s)
Time (s)
hr
day
year

Figure 8. (A-C) Slip evolution (on-fault only) for model geometries shown in Figure 5. The horizontal axis is the cumulative slip on the fault while the vertical axis is the along-fault distance (0 represents the free surface, marked by a red dashed line). The location of the dip change from ramp to décollement is highlighted in gray. The frictional instability nucleation size (h*) and the width of the velocity-weakening region are shown on the right-hand side. Slip is coloured by slip velocity and contoured by slip increment during each phase of the earthquake cycle, where red lines show coseismic increments plotted every 3 s, green lines show postseismic increments plotted every 3 days, and blue lines show interseismic increments plotted every 5 years. (D-F) Maximum slip velocity during a full rupture of the seismogenic zone shown at two scales: the coseismic timescale is shown in seconds (linear scale), while the postseismic timescale is shown with a logarithmic timescale.

3.2.Earthquake sequences with hinge-related OFD

From the incremental inelastic strain computed from the elasto-plastic folding models, and using laboratory-derived friction laws, we show how fault slip and hinge-related OFD evolve in time (Figure 8). Using an adaptive time-stepping solver, we resolve the coseismic, postseismic and interseismic periods of the earthquake cycle. Our results show that earthquakes nucleate near locations where the fault transitions from velocity-weakening to velocity-strengthening friction, and propagate unilaterally in a crack-like manner (Figure 8a-c). As expected for instability ratios of 20-30, we see both system-wide ruptures and partial ruptures of the velocity-weakening region (Barbot, 2019; Cattania, 2019; James R. Rice, 1993). This variability emerges, even on a planar fault, due to the pre-stress state on the fault: when a previous rupture leaves part of the velocity-weakening section under-stressed, propagating ruptures may not be able to overcome the local fracture energy and will terminate. More complicated sequences of earthquakes appear when the up-dip extent of the velocity-weakening region and the ramp-décollement transition overlap (Figure 8b), which may be a consequence of geometric effects of the fault-bend (Li et al., 2018; Ong et al., 2019; Qiu et al., 2016; Sathiakumar et al., 2020).

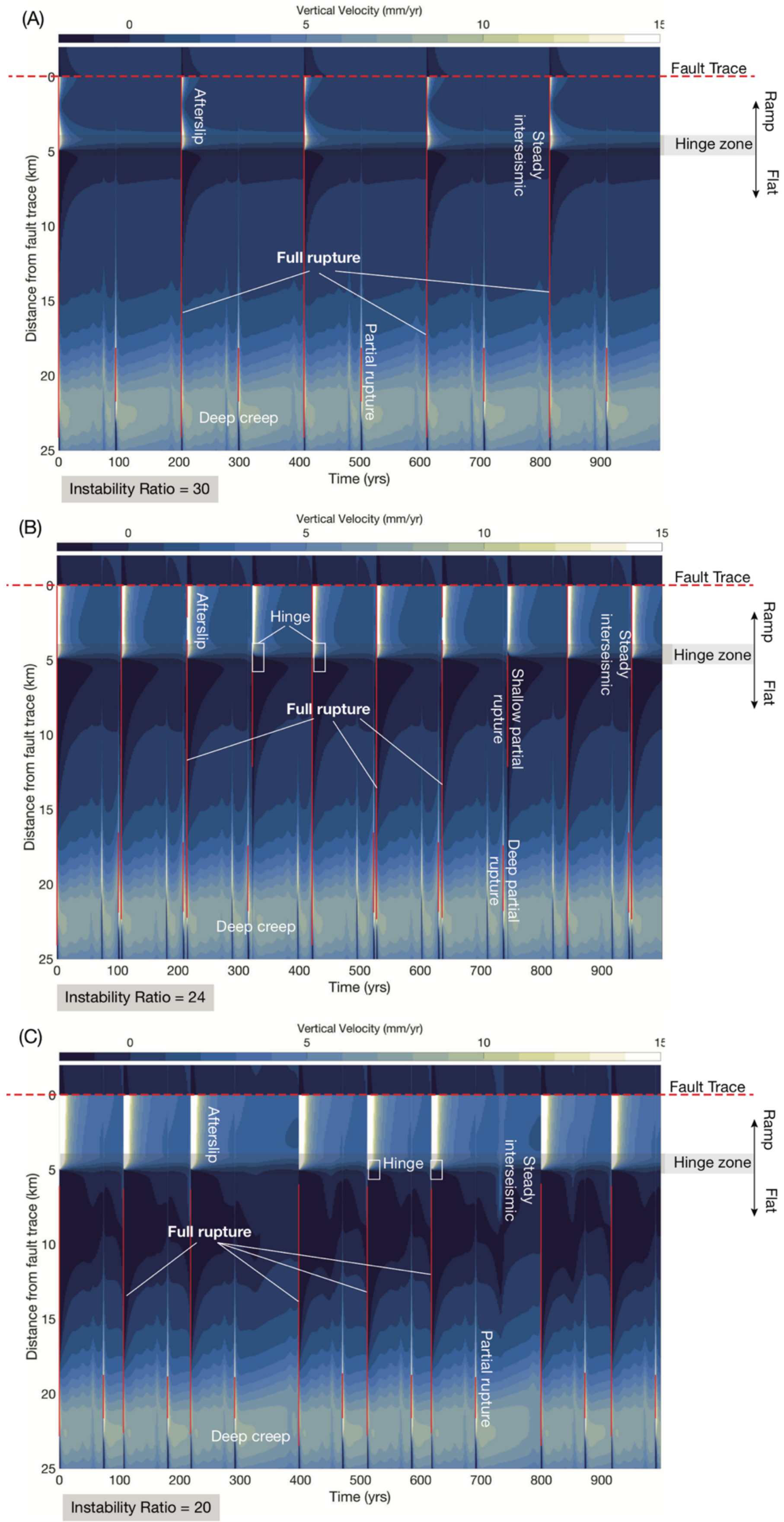

Figure 9. Timeseries of vertical velocity at the surface over a 1000-year period for each of the simulations in Figure 8a-c. Vertical red lines indicate timing and the horizontal extent of coseismic ruptures.

482

Following an earthquake, the velocity-strengthening parts of the fault display afterslip, i.e. stress-driven accelerated creep, in response to the coseismic stress change (Marone et al., 1991; Perfettini & Avouac, 2004). Here, we focus only on afterslip on the shallow velocity-strengthening section of the fault, but note that the deep velocity-strengthening section also creeps postseismically (Figure 8a-c). Since afterslip depends on the magnitude of stress transfer (Marone et al., 1991), only large earthquakes and earthquakes that rupture close to the velocity-strengthening sections can drive a detectable acceleration in the creep rate. This creep may initiate during the earthquake or immediately after the event, and will then decay nearly logarithmically with time (linear on a log-log plot, Figure 8d-f). In addition to on-fault processes, inelastic strain also occurs within the hinge zone. By varying the width of the velocity-weakening region, we can observe how propagating ruptures activate deformation in the hinge region. Hinge-related OFD appears to initiate when the rupture front reaches the ramp-décollement transition, and then evolves similarly to afterslip (Figure 8 d-f). This stress-driven evolution tells us that the aggregate behavior of the hinge follows from slip on the individual bedding layer interfaces, which are governed by velocity-strengthening friction (Table 2).

Typical interpretations of earthquake sequence deformation are based on surface observations. To mimic this, we visualize the vertical displacement rate of the ground surface in response to fold growth over a 1000-year period (Figure 9). In all scenarios, we see peak deformation rates during and immediately after the earthquake. This rapid deformation is followed by a signal that decays in time until the next event that breaks the frontal section of the fault (Figure 9b). Deeper partial ruptures appear as sharp features in the velocity field, but their post-earthquake slip evolution produces only a feeble response in the surface deformation field. We observe large spatial gradients, in the velocity field, near the hinge zone early in the postseismic period following large earthquakes; this gradient diffuses away in time (Figure 9). Late in the interseismic phase, the velocity field appears nearly time-invariant, with a broad uplift peak (long wavelength) over the deeper velocity-weakening to velocity-strengthening transition region on the fault that decays towards the fault extremities (Figure 9). When the shallow velocity-strengthening section of the fault spans the length of the ramp, there is substantial steady interseismic uplift of the anticline (Figure 9b,c). However, in simulations where the velocity-weakening section extends up the ramp and close to the free surface, there is negligible uplift during the long interseismic period (Figure 9a).

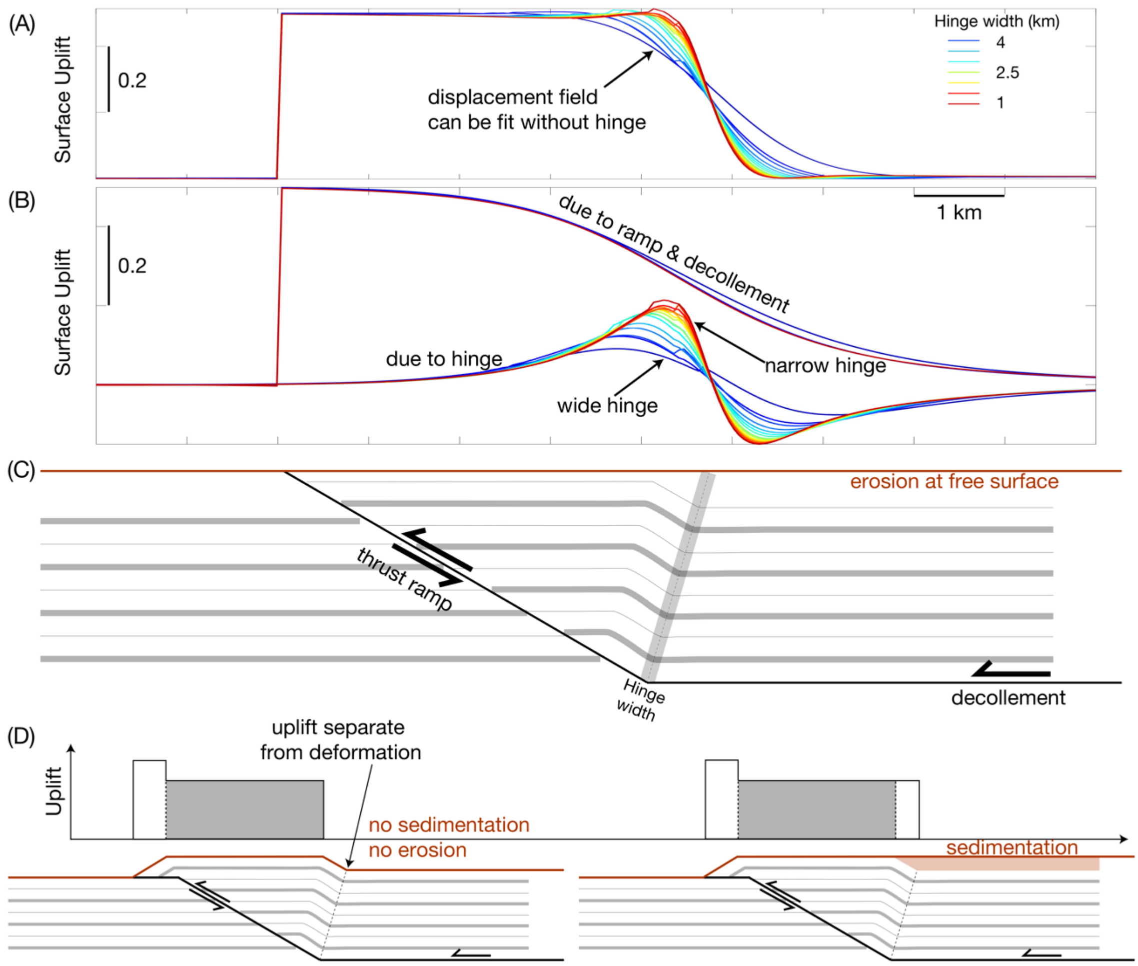

Figure 10. (A) Surface displacement field for growth of a fold over a complete earthquake cycle. The different colored lines show the results of models with different hinge widths. (B) Decomposition of the displacement field into the elastic response of the medium to slip on the ramp-décollement, and due to inelastic strain in the hinge zone. For sufficiently narrow hinges, the surface deformation signal is obvious. However, for a wide hinge, an equivalent elastic solution exists that masks the effect of hinge-related OFD. (C) Underlying geometry of the fault-bend fold. (D) Alternate fold growth models and associated surface uplift. The gray rectangle indicates the uplift pattern expected from the surface erosion model shown in (C).

4. Discussion

We have developed a numerical framework to investigate how hinge-related OFD, in the hanging wall of a fault-cored anticline, evolves with fault slip to grow a fold over timescales ranging from milliseconds to thousands of years. Using elasto-plastic models, we estimate the length-scales and strain rates of hinge-related inelastic deformation (Figure 6,7a). We then use this geometry and a long-term loading rate to run earthquake sequence simulations (Figure 5), with the goal of predicting deformation that can be observed by seismology and geodesy during the various phases of the earthquake cycle (Figure 9). In this section, we use the results of our simulations to discuss why hinge-related OFD is only rarely observed in geodetic data despite its documented role in long-term geological deformation, and how we can modify existing inverse methods to be more sensitive to these processes. We also discuss the impact of hinge-related OFD on the growth of topography.

4.1.How well can we detect ongoing inelastic hinge zone deformation?

Elastic and inelastic (hinge-related OFD) fold growth has been observed at coseismic and postseismic timescales in fold-thrust belt settings (Figure 3b,d; Ainscoe et al., 2017; Béon et al., 2017; Copley, 2014; Copley & Reynolds, 2014; Simon Daout et al., 2021; Gold et al., 2019; Kuo et al., 2014; Zhou et al., 2016, 2018). Flexural slip processes have also been identified related to both dynamic triggering due to passing seismic waves (Kaneko et al., 2015), and steady interseismic deformation (Le Béon et al., 2019; Simon Daout et al., 2019; Mackenzie et al., 2018; Mariniere et al., 2020). However, such observations are infrequent, which is surprising given how ubiquitous fault bends are in sub-surface imaging of fold-thrust belts (Dahlen et al., 1984; Dahlen & Suppe, 1988; Hubbard et al., 2015). And yet, many geodetic observations from thrust settings can be fit satisfactorily by slip on a fault, most often planar, with a purely elastic response of the crust (e.g., Ingleby et al., 2020; Moreno et al., 2009; Page et al., 2011).

From our modeling, we suggest that a significant part of this discrepancy arises due to the existence of an (approximate) equivalent elastic solution to most fold growth surface deformation fields (Figure 10). In other words, the sparsity and noise in the surface deformation data as well as the non-unique solutions in the numerical tools we employ hide the inelastic response of the hanging wall, and therefore allow a purely elastic hanging wall response to fault slip to fit the data sufficiently well. We expound on this in the subsequent paragraphs.

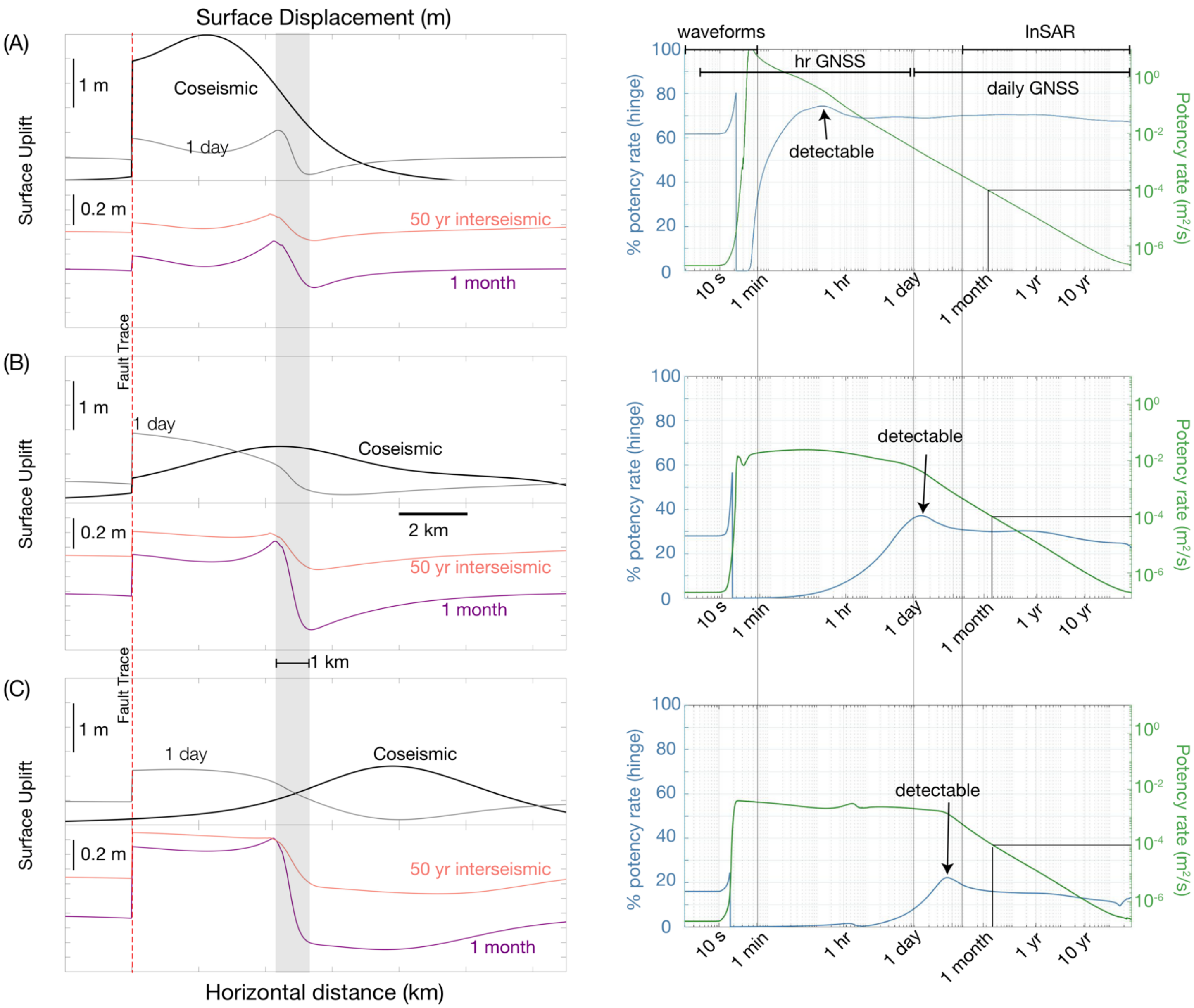

Figure 11. Ease of detection of hinge-related OFD signals during different phases of the earthquake cycle for three representative cases (A-C) highlighted in Figure 7, 8. Left panel shows incremental surface displacements over a number of timespans: immediately after the earthquake (black), 1-day afterslip with coseismic slip removed (gray), differential postseismic deformation in 1 month (purple) since the earthquake (from 1 day to 1 month after the event) and the 50 year interseismic deformation from 10 to 60 years after the earthquake (red). Right panels show % moment or potency rate released by the hinge (blue) and the absolute potency rate (green) versus time. The percentage potency is calculated by considering the total potency released by 10 km of the fault, from the free surface down, and the hinge region. Also highlighted are the typical timescales of observation of different seismo-geodetic methods.

551

4.1.1. High density spatial sampling

In order to discriminate between the elastic and inelastic response of the crust to slip on a ramp-décollement fault based on surface deformation, two basic criteria must be satisfied. First, the surface measurements must be spatially dense enough to capture the displacement gradient near the back-limb of the fold (Figure 10a). Second, these measurements must have a high enough signal-to-noise ratio to successfully discern between the elastic response of the crust to slip on an underlying fault and the combined deformation of the crust due to fault slip and hinge zone deformation (Figure 10b).

Point measurements by many geodetic methods (GNSS, levelling, geodetic surveying), while precise, are unable to capture the spatial scale of hinge-related OFD. Without sufficient observation locations in the hanging wall, the displacement fields due to a purely elastic crust, a narrow hinge, and a wide hinge zone will all appear identical (Allmendinger et al., 2009). This problem can be overcome by using remote sensing methods such as InSAR or cross-correlation of optical images (Avouac & Leprince, 2015; Elliott et al., 2016; Simons & Rosen, 2007). These methods provide estimates of surface deformation with high spatial density sampling but are limited to observations over some arbitrary time period in the earthquake cycle, which can be a problem as fault slip is likely non-uniform in space and time.

4.1.2. Accounting for slip gradients and fault geometry

To identify significant inelastic hinge deformation, when we have sufficiently dense spatio-temporal observations, fitting the surface observations using a purely elastic crust (no hinge zone) must produce spatio-temporally coherent residuals. In other words, it should not be possible to explain the observed surface displacements by either – (1) spatial gradients in fault slip or (2) a modified fault geometry.

Encountering surface displacement fields due to spatial gradients in slip are inevitable. There are no geodetic datasets with sufficient spatio-temporal coverage that can provide us with displacement fields arising from uniform fault slip, a process that would require observations spanning an entire earthquake cycle (100-1000 years). However, the issue arising from alternate fault geometries can be addressed if we use structural information from geomorphic, geological and seismic imaging studies to construct and fix fault geometries (e.g., Avouac, 2015; Le Béon et al., 2014; Chen et al., 2007; Yue et al., 2005).

We note that geologically consistent deformation fields may differ from the predictions from our simulations, due to topographic effects and surface processes (Figure 10d).

Combining such an *apriori* fault geometry model with surface displacement observations from some time period in the earthquake cycle would allow us to assess if there was any inelastic OFD. The key here is that hinge-related OFD would produce large surface displacement gradients in the back limb of the fold, a feature that would generate coherent residuals when the data is fitted with a purely elastic crust model and thereby allow us identify inelastic crustal deformation.

In the following section we expand on how we can detect hinge-related OFD from geodetic observations that do not span an entire seismic cycle but are limited to a narrow snapshot in time.

4.2.Surface observations of OFD modulated by the earthquake cycle

High spatio-temporal resolution geophysical observations only go back a couple decades, which is insufficient to observe the full earthquake cycle. Thus, in order to detect hinge-related OFD, we need to not only have appropriate observations, but also a geological setting with the right conditions (Figure 10), and the right time interval. For example, consider the 1999 Chi-Chi earthquake: the static displacement field derived from remote sensing (Kuo et al., 2014) shows clear elastic and inelastic hanging wall deformation (Figure 3a-b). However, without information about the temporal evolution of strain, we cannot distinguish OFD that occurred coseismically from OFD that occurred in the hours and days after the event.

In this section, we discuss how our numerical simulations of earthquake sequence deformation can guide the use of multiple observational methods to detect hanging wall deformation processes. To visualize these effects, we plot the surface displacement field during different parts of the earthquake cycle, along with the potency (moment) released by the hinge for three representative cases (Figure 11; earthquake sequence simulations in Figure 8).

4.2.1. Coseismic and early postseismic

Not all earthquakes drive hinge-related OFD in the same way. For example, partial ruptures generally do not drive any hinge-related OFD, whereas earthquakes that rupture the entire fault cause significant folding and produce an observable displacement gradient near the hinge both coseismically and postseismically (Figure 8,9). This is because earthquakes that are small or far from the hinge, transfer negligible stress to the bedding plane faults that constitute the hinge. Since fault slip rates are controlled by their stress state, due to velocity-dependent frictional strength (Dieterich, 1979; Scholz, 1998), the hinge remains unperturbed by partial ruptures. For large earthquakes that can transfer sufficient stress to the hinge zone (on the order of MPa), the optimal timescale at which displacement gradients associated with OFD are observable ranges from immediately after the earthquake to months later (Figure 11a-c). The coseismic period, however, is unsuitable for OFD observations, because the deformation due to on-fault slip is orders of magnitude greater than hinge-related OFD (Figure 11).

In light of our results, the coseismic folding example from the 1999 Chi-Chi earthquake we highlighted earlier (Figure 3a-b), may in fact be the effect of rapid early postseismic deformation (Figure 11a). With only a snapshot of deformation computed from optical images obtained days before and after the earthquake, we can only set bounds on how fast hinge-related OFD may have occurred; OFD may have occurred at a rate between meters/day to meters/second. Detecting the evolution of such rapid hinge deformation during the minutes and hours following the earthquake may require the development of new techniques. While waveform data from seismometers and high rate GNSS are sensitive to the coseismic rupture process, high rate GNSS observations decimated at the minute to hourly scale contain additional information about slower processes that deform the medium, but do not release seismically detectable radiation (Figure 11). Thus, both types of data contain the rupture process, but they differ in their sensitivity to slower deformation. Joint kinematic inversions of earthquake source parameters typically pool waveforms and geodetic observations to obtain average parameters (Fukuda & Johnson, 2010; Funning et al., 2014; Yabuki & Matsu'ura, 1992), which diminishes our ability to estimate early afterslip. Instead, we suggest partial pooling of these datasets, which is a popular machine learning method to take advantage of datasets that contain similar information on average but differ in statistically coherent ways (Gelman & Hill, 2006). Alternatively, it may also be possible to detect hinge deformation by explicitly inverting for rapid early afterslip in addition to coseismic slip (Milliner et al., 2020; Ragon et al., 2019).

4.2.2. Postseismic

For cases where hinge-related OFD is only detectable at the week to month timescale, GNSS observations at the daily scale and InSAR may help constrain the rates and styles of OFD (Figure 11c). This is the case for décollement ruptures (Figure 11c, 9c; slip evolution is shown in Figure 8c), Both daily GNSS and InSAR are sensitive to the same process and can be pooled to reveal the temporal variation of deformation associated with the fault and the hinge. At timescales longer than years and decades, the postseismic deformation field decays to a background low amplitude interseismic velocity (Figure 9, 11).

From a theoretical perspective, these observational timescales vary inversely with the long-term loading rate ($\dot{s}^{\infty}$) and the shear modulus of the medium (G), which we chose as 10^{-9} m/s and 10 GPa in the simulations. The relaxation timescale of afterslip for velocity-strengthening faults can be estimated from spring-slider analysis as $t_R = \frac{(a-b)\bar{\sigma}}{\dot{\tau}^{\infty}}$ (Perfettini & Avouac, 2004); $\dot{\tau}^{\infty}$ is the long-term loading rate, and has a linear dependence on $\dot{s}^{\infty}$ and G (Equation 2, 7). This means that the timescales shown in Figure 11 need to be adjusted based on the effective loading of the fault in question.

Take for example the case of the Kurit fold (Figure 3c-d), where we observe temporally decaying afterslip and hinge deformation forty years after the last known earthquake (Zhou et al., 2016, 2018). While this may appear surprising compared to typical detectable afterslip (1-5 years, Helmstetter & Shaw, 2009; Ingleby & Wright, 2017), it can be explained by the fact that the long-term slip rate on the frontal faults in the Tabas fold-belt is only 1-2 mm/yr (<10^{-10} m/s), and the surrounding materials have low rigidity (Walker et al., 2015; Zhou et al., 2018). These properties result in an effective loading rate that is an order of magnitude lower than our simulations, and therefore the afterslip signal remains discernable over decades rather than the years that we predicted in our simulations.

4.2.3. Interseismic

During the interseismic period, detecting slow fold growth requires a shallow ramp that is able to creep (in order to generate displacement gradients). In most fold-thrust belts, the steady-state creep rates on ramps are limited by the stress shadow cast by down-dip fault locking (Almeida et al., 2018; Herman et al., 2018), which significantly reduces the stress accumulation rate updip, on both primary faults and within a hinge zone. While there are some notable local examples of steady creep-driven fold growth (Le Béon et al., 2019; Simon Daout et al., 2019; Mackenzie et al., 2018; Mariniere et al., 2020), frontal folds in large fold-thrust belts do not usually show substantial interseismic creep (e.g., in the Himalayas and the

Indo-Burman fold-belts, Grandin et al., 2012; Lindsey et al., 2018; Mallick et al., 2019, 2020). Since steady creep rates are typically slow, detecting OFD also requires a long time-window to accrue detectable displacements (Figure 11).

Even when interseismic OFD is present, it can be hard to detect. This is because the long wavelength signals related to fault locking and deep creep dominate the surface deformation signal during the interseismic period (Figure 9). If the interseismic creep signal is time-invariant, it mostly reflects the background loading process; as a result, such a signal is unlikely to provide any information about the evolution of the stress state or material properties. In general, detailed inferences about creeping or frictionally locked regions during the interseismic period are difficult due to the combined effects of the stress shadow from frictional locking on the fault and the limit of resolution relative to the noise floor (Almeida et al., 2018; Herman et al., 2018).

4.3.Building geologic structure and topography

Slip over a fault bend necessarily builds topography in the long term. This is apparent even for a purely elastic medium responding to slip over a ramp-décollement system (displacement profile in Figure 1b). In this case, deep interseismic creep (representing far-field horizontal shortening) causes long-wavelength uplift of the medium (Figure 9), while slip on the ramp-décollement causes uplift of the hanging wall above the ramp, with subsidence both downdip of the ramp and in the footwall close to the fault (Figure 10b). In addition to large-scale uplift of the hanging wall, OFD in the hinge zone can permanently deform the hanging wall over a narrow length-scale, producing a fold scarp (Figure 10).

Based on our modeling, a significant portion of topographic growth due to hinge-related OFD is coseismic (Fig. 11: the hinge potency rate is highest during earthquakes). However, the work associated with this process is orders of magnitude smaller than concurrent fault slip, and hence it is difficult to disentangle this signal from a purely elastic crustal response to fault slip using observational techniques. Permanent deformation near the hinge only becomes detectable as on-fault processes slow down to match the rate of moment release by hinge-related OFD, as discussed in Section 4.2, but these OFD processes and related topographic growth occur continuously throughout the earthquake cycle. Our simulations show that more than 50% of the total potency associated with hinge zone OFD occurs within the first month after the earthquake (Figure 11).

Long wavelength interseismic uplift has been detected in a number of geodetically monitored convergent margins, peaking over the coastline or shelf break (in subduction zones), or where topography is high (collisional boundaries). As a result, studies have interpreted that mountain building may be a relatively time-invariant process largely occurring during the interseismic period (Grandin et al., 2012; Jolivet et al., 2020; Malatesta et al., 2020; Meade, 2010; Saillard et al., 2017). Based on our results, we suggest a more complicated model of mountain building. Different physical mechanisms operate over the different spatial zones that constitute a convergent margin, with accretion and fold growth within the fold-thrust belt, following brittle mechanics (Dahlen, 1990; Dahlen et al., 1984), and friction to flow-like processes beyond the backstop of the fold belt and above the deepest parts of the megathrust (Agard et al., 2018). Topography building due to fault slip and hinge-related OFD represents how mountains are built in the brittle regime: one-fold at a time. It may be true that coastal uplift and the growth of high topography does occur interseismically, but further study is needed to understand how friction and flow processes operate together on the deep megathrust to build topography at the larger scale (Van Dinther et al., 2013; Menant et al., 2020).

4.4.Including hinge-related OFD in numerical simulations and inverse models

The past few years have seen a push towards incorporating geological and geodynamic considerations into earthquake simulations and seismic hazard models (e.g., Dal Zilio et al., 2019; Sathiakumar et al., 2020; van Zelst et al., 2019). However, resolving the complexity of earthquakes, which evolve on the millisecond timescale, with a fold-thrust belt growing over million years is a daunting task (van Zelst et al., 2019). The major difficulties that arise are: resolving the complexity of frictional instabilities with an appropriate spatiotemporal grid, and accounting for pervasive inelastic deformation within the bulk medium.

In this study, we separate the two timescales and use a one-way coupling from the geological timescale to the earthquake sequence timescale (Figure 5), thereby accounting for both timescales while preserving kinematic and mechanical consistency. We show that permanent deformation of the hanging wall occurs in a narrow band, with length-scales that are controlled by the angularity of the fault-bend and the flexibility/bending resistance of the hanging wall (Figure 7). Our computational cost is only mildly greater than for typical earthquake sequence simulations, since we need only explicitly define regions of inelastic strain, allowing the rest of the bulk medium to remain a linear elastic solid with no meshing. The off-fault response effectively becomes a time-varying loading rate term for the on-fault stress evolution in Equation 7. Variations in loading rates have been noted to affect earthquake nucleation sites and sizes in recent earthquake sequence simulations for fold-thrust belt settings (Sathiakumar et al., 2020). It remains to be investigated if including time-varying loading due to hinge related OFD significantly impacts the statistical behavior of earthquake sequences and the properties of aseismic phenomena, such as scaling relationships between stress drop and magnitude, rupture velocities and the radiation efficiency of fast seismic events, and the duration and propagation velocity of afterslip and other postseismic processes.

For kinematic inverse problems, hinge-related OFD can be approximated by borrowing concepts from plate motion kinematics, i.e. closing the velocity vector diagram of a triple junction formed by a ramp, décollement and hinge, collapsed onto a fault plane (e.g., S. Daout et al., 2016; Sathiakumar et al., 2020; Souter & Hager, 1997). These studies take advantage of the ambiguity in direction of shear (inelastic strain) associated with shear bands. In other words, the displacement and stress fields generated by backthrust deformation are nearly identical to those produced by slip on a series of bedding plane contacts in a hinge zone (see focal mechanisms in Figure 4c). This approximation is a solution for inverse problems aimed at inferring slip/strain from surface displacements, but creates a number of issues in the stress formulation needed to simulate earthquake sequences: (1) An infinitesimally narrow fault bend, which is a pre-requisite for the backthrust approximation, creates an impossible physical situation in a purely elastic medium – interpenetration of the medium around the fault junction (Romanet, 2020); (2) as a result, the on-fault traction kernel (Equation 2) has a singularity at the fault bend that dramatically alters the tractions on the fault; and (3) it is difficult to choose an appropriate constitutive relation for the backthrust, considering that it does not exist. As a result, we recommend using this approximation for inverse problems but not for earthquake sequence simulations.

5. Conclusions

Fault bends create unbalanced elastic stresses in the medium that grow with slip on the fault. These stresses are relaxed by permanent or inelastic off-fault deformation (OFD) of the hanging wall. In the layered sedimentary rocks typically observed in fold-thrust belts, this inelastic OFD takes the form of a hinge zone, a process described by fault-bend folding theory. Although evidence for inelastic hinge-related OFD is ubiquitous in geologic and geomorphological data, it is difficult to observe the OFD process in seismo-geodetic datasets.

In this article, we present a unified modeling strategy for earthquake sequence simulations and long-term fold growth in the brittle crust that accounts for the mechanical coupling between fault slip and inelastic strain in the hanging wall. We show that it is difficult to identify inelastic behaviour of the crust in seismological and geodetic data, largely because of the existence of equivalent elastic solutions to surface deformation data. This problem and the associated non-uniqueness issue arise from (1) poorly known fault geometries and elastic properties of the crust, and (2) insufficient spatial and temporal sampling of earthquake-cycle modulated surface deformation data.

Hinge-related OFD and fault slip are sources of permanent crustal deformation, leading to the growth of topography. Topography and geologic structure, at least at the scale of individual anticlines, are built throughout the earthquake cycle. The rate of this process is strongly modulated by the rate of on-fault moment release, which means hinge-related OFD is fastest during and immediately after large earthquakes and the rate decays logarithmically in time. However, concurrent fault slip generates a significantly larger signal in observational datasets, thereby obfuscating the inelastic deformation near the hinge. Observing and isolating geodetic signals of hinge-related OFD is possible when the on-fault moment release decreases to values comparable to the off-fault moment release; this is most likely in the postseismic period. We highlight this for the two examples we have considered in this study – (1) rapid hinge-related OFD, at velocities possibly exceeding meters/day, following the 1991 M_w 7.6 Chi-Chi earthquake in Taiwan, captured by optical imagery acquired days before and after the event; (2) slow and long-lived hinge-related OFD, at rates of millimeters/year, following the 1978 M_w 7.3 Tabas-e-Golshan earthquake in Iran, imaged by InSAR over decades (Figure 3). Therefore, to infer the mechanics of how earthquake-cycle stresses fold the brittle crust, we suggest combining structural geological methods of inferring fault geometry with seismo-geodetic observations from the postseismic period.

6. Acknowledgements

All figures in this paper were made using Generic Mapping Tools (http://doi.wiley.com/10.1029/98EO00426) and MATLAB. The code used and the model outputs are available at (insert NTU-DR link at time pf publication). This research was supported by the Earth Observatory of Singapore and the National Research Foundation Singapore and the Singapore Ministry of Education under the Research Centres of Excellence initiative. This study and associated visits at UC Berkeley were partly funded by the Stephen Riady Geoscience Scholars Fund awarded to RM for the period June 2019 – March 2020. The authors thank Yu-Ting Kuo, Alex Copley and Yu Zhou for sharing data (plotted in Figure 3). RM thanks Emma Hill for her mentorship and for help with writing the proposal for this study, Valère Lambert and Eric Lindsey for discussions about earthquake sequence simulations, Richard Walker and Yu Zhou for early discussions about the Tabas fold belt, and Kyle Bradley for feedback and discussions on various topics presented in this study.

7. References

Agard, P., Plunder, A., Angiboust, S., Bonnet, G., & Ruh, J. (2018). The subduction plate interface: rock record and mechanical coupling (from long to short timescales). *Lithos*, *320–321*, 537–566. https://doi.org/10.1016/j.lithos.2018.09.029

Ainscoe, E. A., Elliott, J. R., Copley, A., Craig, T. J., Li, T., Parsons, B. E., & Walker, R. T. (2017). Blind Thrusting, Surface Folding, and the Development of Geological Structure in the M w 6.3 2015 Pishan (China) Earthquake. *Journal of Geophysical Research: Solid Earth*, *122*(11), 9359–9382. https://doi.org/10.1002/2017JB014268

Allmendinger, R. W., Loveless, J. P., Pritchard, M. E., & Meade, B. (2009). From decades to epochs: Spanning the gap between geodesy and structural geology of active mountain belts. *Journal of Structural Geology*, *31*(11), 1409–1422. https://doi.org/10.1016/j.jsg.2009.08.008

Almeida, R., Lindsey, E. O., Bradley, K., Hubbard, J., Mallick, R., & Hill, E. M. (2018). Can the Updip Limit of Frictional Locking on Megathrusts be Detected Geodetically? Quantifying the Effect of Stress Shadows on Near-Trench Coupling. *Geophysical Research Letters*, *45*(10), 4754–4763. https://doi.org/10.1029/2018GL077785

Avouac, J. P. (2015). *Mountain Building: From Earthquakes to Geologic Deformation. Treatise on Geophysics* (2nd ed., Vol. 6). Elsevier B.V. https://doi.org/10.1016/B978-0-444-53802-4.00120-2

Avouac, J. P., & Leprince, S. (2015). *Geodetic Imaging Using Optical Systems. Treatise on Geophysics: Second Edition* (Vol. 3). Elsevier B.V. https://doi.org/10.1016/B978-0-444-53802-4.00067-1

Barbot, S. (2019). Slow-slip, slow earthquakes, period-two cycles, full and partial ruptures, and deterministic chaos in a single asperity fault. *Tectonophysics*, *768*(March), 228171. https://doi.org/10.1016/j.tecto.2019.228171

Le Béon, M., Suppe, J., Jaiswal, M. K., Chen, Y.-G., & Ustaszewski, M. E. (2014). Deciphering cumulative fault slip vectors from fold scarps: Relationships between long-term and coseismic deformations in central Western Taiwan. *Journal of Geophysical Research: Solid Earth*, *119*(7), 5943–5978. https://doi.org/10.1002/2013JB010794

Béon, M. Le, Huang, M.-H., Suppe, J., Huang, S.-T., Pathier, E., Huang, W.-J., et al. (2017). Shallow geological structures triggered during the Mw 6.4 Meinong earthquake, southwestern Taiwan. *Terrestrial, Atmospheric and Oceanic Sciences*, *28*(5), 663–681. https://doi.org/10.3319/TAO.2017.03.20.02

Le Béon, M., Marc, O., Suppe, J., Huang, M. H., Huang, S. T., & Chen, W. S. (2019). Structure and

Deformation History of the Rapidly Growing Tainan Anticline at the Deformation Front of the Taiwan Mountain Belt. *Tectonics*, *38*(9), 3311–3334. https://doi.org/10.1029/2019TC005510

Berger, P., & Johnson, A. M. (1980). First-order analysis of deformation of a thrust sheet moving over a ramp. *Tectonophysics*, *70*(3–4). https://doi.org/10.1016/0040-1951(80)90276-0

Biot, M. A. (1961). Theory of Folding of Stratified Viscoelastic Media and Its Implications in Tectonics and Orogenesis, (November), 1595–1620.

Biot, M. A. (1964). THEORY OF INTERNAL BUCKLING OF A CONFINED MULTILAYERED STRUCTURE. *GSA Bulletin*, *75*, 563–568. https://doi.org/10.1007/bf00203353

Blanpied, M. L., Lockner, D. A., & Byerlee, J. D. (1995). Frictional slip of granite at hydrothermal conditions. *Journal of Geophysical Research*, *100*(B7). https://doi.org/10.1029/95jb00862

Brandes, C., & Tanner, D. C. (2014). Fault-related folding: A review of kinematic models and their application. *Earth-Science Reviews*, *138*, 352–370. https://doi.org/10.1016/j.earscirev.2014.06.008

Bruhat, L., & Segall, P. (2016). Coupling on the northern Cascadia subduction zone from geodetic measurements and physics-based models. *Journal of Geophysical Research: Solid Earth*, *121*(11), 8297–8314. https://doi.org/10.1002/2016JB013267

Butler, R. W. H., Bond, C. E., Cooper, M. A., & Watkins, H. (2020). Fold–thrust structures – Where have all the buckles gone? *Geological Society Special Publication*, *487*(1), 21–44. https://doi.org/10.1144/SP487.7

Cattania, C. (2019). Complex Earthquake Sequences On Simple Faults. *Geophysical Research Letters*, (May), 2019GL083628. https://doi.org/10.1029/2019GL083628

Chen, Y. G., Lai, K. Y., Lee, Y. H., Suppe, J., Chen, W. S., Lin, Y. N. N., et al. (2007). Coseismic fold scarps and their kinematic behavior in the 1999 Chi-Chi earthquake Taiwan. *Journal of Geophysical Research: Solid Earth*, *112*(3), 1–15. https://doi.org/10.1029/2006JB004388

Copley, A. (2014). Postseismic afterslip 30 years after the 1978 Tabas-e-Golshan (Iran) earthquake: Observations and implications for the geological evolution of thrust belts. *Geophysical Journal International*, *197*(2), 665–679. https://doi.org/10.1093/gji/ggu023

Copley, A., & Reynolds, K. (2014). Imaging topographic growth by long-lived postseismic afterslip at Sefidabeh, east Iran. *Tectonics*, *33*(3), 330–345. https://doi.org/10.1002/2013TC003462

Cosgrove, J. W. (2015). The association of folds and fractures and the link between folding, fracturing and fluid flow during the evolution of a fold-thrust belt: A brief review. *Geological Society Special Publication*, *421*(1), 41–68. https://doi.org/10.1144/SP421.11

Dahlen, F. A. (1990). Critical Taper Model of Fold-And-Thrust Belts and Accretionary Wedges. *Annual Review of Earth and Planetary Sciences*, *18*(1), 55–99. https://doi.org/10.1146/annurev.ea.18.050190.000415

Dahlen, F. A., & Suppe, J. (1988). Mechanics, growth, and erosion of mountain belts. *Geological Society of America Special Papers*, *218*(October), 161–178. https://doi.org/10.1130/SPE218-p161

Dahlen, F. A., Suppe, J., & Davis, D. (1984). Mechanics of fold-and-thrust belts and accretionary wedges: Cohesive Coulomb Theory. *Journal of Geophysical Research*, *89*(B12), 10087–10,101. https://doi.org/10.1029/JB089iB12p10087

Dal Zilio, L., van Dinther, Y., Gerya, T., & Avouac, J. P. (2019). Bimodal seismicity in the Himalaya controlled by fault friction and geometry. *Nature Communications*, *10*(1), 48. https://doi.org/10.1038/s41467-018-07874-8

Daout, S., Barbot, S., Peltzer, G., Doin, M. P., Liu, Z., & Jolivet, R. (2016). Constraining the kinematics of metropolitan Los Angeles faults with a slip-partitioning model. *Geophysical Research Letters*, *43*(21), 11,192-11,201. https://doi.org/10.1002/2016GL071061

Daout, Simon, Sudhaus, H., Kausch, T., Steinberg, A., & Dini, B. (2019). Interseismic and Postseismic Shallow Creep of the North Qaidam Thrust Faults Detected with a Multitemporal InSAR Analysis. *Journal of Geophysical Research: Solid Earth*, 2019JB017692. https://doi.org/10.1029/2019JB017692

Daout, Simon, Parsons, B., & Walker, R. (2021). Post-Earthquake Fold Growth Imaged in the Qaidam basin, China, With InSAR. *Journal of Geophysical Research: Solid Earth*. https://doi.org/10.1029/2020JB021241

Dieterich, J. H. (1979). Modeling of Rock Friction Experimental 1. Results and Constitutive Equations. *Journal of Geophysical Research*, *84*(9), 2161–2168. Retrieved from http://dx.doi.org/10.1007/BF00876539%5Cnhttp://www.agu.org/pubs/crossref/1979/JB084iB05p02161.shtml

Van Dinther, Y., Gerya, T. V., Dalguer, L. A., Mai, P. M., Morra, G., & Giardini, D. (2013). The seismic cycle at subduction thrusts: Insights from seismo-thermo- mechanical models. *Journal of Geophysical Research: Solid Earth*, *118*(12), 6183–6202. https://doi.org/10.1002/2013JB010380

Dunham, E. M., Belanger, D., Cong, L., & Kozdon, J. E. (2011). Earthquake ruptures with strongly rate-weakening friction and off-fault plasticity, part 2: Nonplanar faults. *Bulletin of the Seismological Society of America*, *101*(5), 2308–2322. https://doi.org/10.1785/0120100076

Elliott, J. R. R., Walters, R. J. J., & Wright, T. J. J. (2016). The role of space-based observation in understanding and responding to active tectonics and earthquakes. *Nature Communications*, *7*(1), 13844. https://doi.org/10.1038/ncomms13844

Fletcher, R. C. (1977). Folding of a single viscous layer: Exact Infinitesimal-Amplitude Solution. *Tectonophysics*, *39*, 593–606.

Fukuda, J., & Johnson, K. M. (2010). Mixed linear-non-linear inversion of crustal deformation data: Bayesian inference of model, weighting and regularization parameters. *Geophysical Journal International*, *181*(3), 1441–1458. https://doi.org/10.1111/j.1365-246X.2010.04564.x

Funning, G. J., Fukahata, Y., Yagi, Y., & Parsons, B. (2014). A method for the joint inversion of geodetic and seismic waveform data using ABIC: Application to the 1997 manyi, tibet, earthquake. *Geophysical Journal International*, *196*(3), 1564–1579. https://doi.org/10.1093/gji/ggt406

Gelman, A., & Hill, J. (2006). *Data Analysis Using Regression and Multilevel/Hierarchical Models. Data Analysis Using Regression and Multilevel/Hierarchical Models*. https://doi.org/10.1017/cbo9780511790942

Gold, R. D., Clark, D., Barnhart, W. D., King, T., Quigley, M., & Briggs, R. W. (2019). Surface Rupture and Distributed Deformation Revealed by Optical Satellite Imagery: The Intraplate 2016 M w 6.0 Petermann Ranges Earthquake, Australia . *Geophysical Research Letters*, (May 2016). https://doi.org/10.1029/2019gl084926

Grandin, R., Doin, M. P., Bollinger, L., Pinel-Puysségur, B., Ducret, G., Jolivet, R., & Sapkota, S. N. (2012). Long-term growth of the Himalaya inferred from interseismic InSAR measurement. *Geology*, *40*(12), 1059–1062. https://doi.org/10.1130/G33154.1

Gratier, J. P., Renard, F., & Labaume, P. (1999). How pressure solution creep and fracturing processes interact in the upper crust to make it behave in both a brittle and viscous manner. *Journal of Structural Geology*, *21*(8–9), 1189–1197. https://doi.org/10.1016/S0191-8141(99)00035-8

Gratier, J. P., Dysthe, D. K., & Renard, F. (2013). *The Role of Pressure Solution Creep in the Ductility of the Earth's Upper Crust*. *Advances in Geophysics* (Vol. 54). Elsevier Inc. https://doi.org/10.1016/B978-0-12-380940-7.00002-0

Gregg Erickson, S., & Jamison, W. R. (1995). Viscous-plastic finite-element models of fault-bend folds. *Journal of Structural Geology*, *17*(4), 561–573. https://doi.org/10.1016/0191-8141(94)00082-B

Gregg Erickson, S., Strayer, L. M., & Suppe, J. (2005). Numerical modeling of hinge-zone migration in fault-bend folds. *AAPG Memoir*, (82), 438–452. https://doi.org/10.1306/m82813c23

Helmstetter, A., & Shaw, B. E. (2009). Afterslip and aftershocks in the rate-and-state friction law. *Journal of Geophysical Research: Solid Earth*, *114*(B1). https://doi.org/10.1029/2007JB005077

Herman, M. W., Furlong, K. P., & Govers, R. (2018). The Accumulation of Slip Deficit in Subduction Zones in the Absence of Mechanical Coupling: Implications for the Behavior of Megathrust Earthquakes. *Journal of Geophysical Research: Solid Earth*, *123*(9), 8260–8278. https://doi.org/10.1029/2018JB016336

Honea, E., & Johnson, A. M. (1976). A THEORY OF CONCENTRIC , KINK AND SINUSOIDAL FOLDING AND OF MONOCLINAL FLEXURING OF COMPRESSIBLE , ELASTIC This fourth part of our series of papers * on folding of elastic multilayers primarily deals with folds in multi ~ yers subjected to princi ~~ civil, *30*, 197–239.

Huang, W.-J., & Johnson, K. M. (2016). A Fault-Cored Anticline Boundary Element Model Incorporating the Combined Fault Slip and Buckling Mechanisms. *Terrestrial, Atmospheric and Oceanic Sciences*, *27*(1), 073. https://doi.org/10.3319/TAO.2015.06.18.01(TT)

Hubbard, J., Barbot, S., Hill, E. M., & Tapponnier, P. (2015). Coseismic slip on shallow décollement megathrusts: Implications for seismic and tsunami hazard. *Earth-Science Reviews*, *141*(November), 45–55. https://doi.org/10.1016/j.earscirev.2014.11.003

Ingleby, T., & Wright, T. J. (2017). Omori-like decay of postseismic velocities following continental earthquakes. *Geophysical Research Letters*, *44*(7), 3119–3130. https://doi.org/10.1002/2017GL072865

Ingleby, T., Wright, T. J., Hooper, A., Craig, T. J., & Elliott, J. R. (2020). Constraints on the geometry and frictional properties of the Main Himalayan Thrust using co-, post- and interseismic deformation in Nepal. *Journal of Geophysical Research: Solid Earth*, 1–26. https://doi.org/10.1029/2019jb019201

Jackson, M., & Bilham, R. (1994). Constraints on Himalayan deformation inferred from vertical velocity fields in Nepal and Tibet. *Journal of Geophysical Research*, *99*(B7), 13897–13912. https://doi.org/10.1029/94JB00714

Johnson, A. M., & Berger, P. (1989). Kinematics of fault-bend folding. *Engineering Geology*, *27*(1–4), 181–200. https://doi.org/10.1016/0013-7952(89)90033-1

Johnson, A. M., & Pfaff, V. J. (1989). Parallel, similar and constrained folds. *Engineering Geology*, *27*(1–4), 115–180. https://doi.org/10.1016/0013-7952(89)90032-X

Johnson, K. M. (2018). Growth of Fault-Cored Anticlines by Flexural Slip Folding: Analysis by Boundary Element Modeling. *Journal of Geophysical Research: Solid Earth*, *123*(3), 2426–2447. https://doi.org/10.1002/2017JB014867

Jolivet, R., Simons, M., Duputel, Z., Olive, J. -A., Bhat, H. S., & Bletery, Q. (2020). Interseismic Loading of Subduction Megathrust Drives Long-Term Uplift in Northern Chile. *Geophysical Research Letters*, *47*(8), 1–11. https://doi.org/10.1029/2019gl085377

Kanda, R. V. S., & Simons, M. (2010). An elastic plate model for interseismic deformation in subduction zones. *Journal of Geophysical Research: Solid Earth*, *115*(3), 1–19. https://doi.org/10.1029/2009JB006611

Kaneko, Y., Hamling, I. J., Van Dissen, R. J., Motagh, M., & Samsonov, S. V. (2015). InSAR imaging of displacement on flexural-slip faults triggered by the 2013 Mw 6.6 Lake Grassmere earthquake, central New Zealand. *Geophysical Research Letters*, *42*(3), 781–788. https://doi.org/10.1002/2014GL062767

Kuo, Y.-T., Ayoub, F., Leprince, S., Chen, Y.-G., Avouac, J.-P., Shyu, J. B. H., et al. (2014). Coseismic thrusting and folding in the 1999 M w 7.6 Chi-Chi earthquake: A high-resolution approach by aerial photos taken from Tsaotun, central Taiwan. *Journal of Geophysical Research: Solid Earth*, *119*(1), 645–660. https://doi.org/10.1002/2013JB010308

Li, S., Barnhart, W. D., & Moreno, M. (2018). Geometrical and Frictional Effects on Incomplete Rupture and Shallow Slip Deficit in Ramp-Flat Structures. *Geophysical Research Letters*, 1–9. https://doi.org/10.1029/2018GL079185

Lindsey, E. O., Almeida, R., Mallick, R., Hubbard, J., Bradley, K., Tsang, L. L. H., et al. (2018). Structural Control on Downdip Locking Extent of the Himalayan Megathrust. *Journal of Geophysical Research: Solid Earth*, *123*(6), 5265–5278. https://doi.org/10.1029/2018JB015868

Mackenzie, D., Walker, R., Abdrakhmatov, K., Campbell, G., Carr, A., Gruetzner, C., et al. (2018). A creeping intracontinental thrust fault: past and present slip-rates on the Northern edge of the Tien Shan, Kazakhstan. *Geophysical Journal International*, *215*(2), 1148–1170. https://doi.org/10.1093/gji/ggy339

Malatesta, L. C., Bruhat, L., Finnegan, N. J., & Olive, J. L. (2020). Co-location of the downdip end of seismic coupling and the continental shelf break. *Journal of Geophysical Research: Solid Earth*. https://doi.org/10.1029/2020jb019589

Mallick, R., Lindsey, E. O., Feng, L., Hubbard, J., Banerjee, P., & Hill, E. M. (2019). Active Convergence of the India-Burma-Sunda Plates Revealed by a New Continuous GPS Network. *Journal of Geophysical Research: Solid Earth*, *124*(3), 3155–3171. https://doi.org/10.1029/2018JB016480

Mallick, R., Hubbard, J. A., Lindsey, E. O., Bradley, K. E., Moore, J. D. P., Ahsan, A., et al. (2020). Subduction initiation and the rise of the Shillong Plateau. *Earth and Planetary Science Letters*, *543*, 116351. https://doi.org/10.1016/j.epsl.2020.116351

Mariniere, J., Nocquet, J.-M., Beauval, C., Champenois, J., Audin, L., Alvarado, A., et al. (2020). Geodetic evidence for shallow creep along the Quito fault, Ecuador. *Geophysical Journal International*, *220*(3), 2039–2055. https://doi.org/10.1093/gji/ggz564

Marone, C. J., Scholtz, C. H., & Bilham, R. (1991). On the mechanics of earthquake afterslip. *Journal of Geophysical Research*, *96*(B5), 8441–8452. https://doi.org/10.1029/91JB00275

Mavrommatis, A. P., Segall, P., & Johnson, K. M. (2017). A Physical Model for Interseismic Erosion of Locked Fault Asperities. *Journal of Geophysical Research: Solid Earth*, *122*(10), 8326–8346. https://doi.org/10.1002/2017JB014533

Meade, B. J. (2010). The signature of an unbalanced earthquake cycle in Himalayan topography? *Geology*, *38*(11), 987–990. https://doi.org/10.1130/G31439.1

Menant, A., Angiboust, S., Gerya, T., Lacassin, R., Simoes, M., & Grandin, R. (2020). Transient stripping of subducting slabs controls periodic forearc uplift. *Nature Communications*, *11*(1), 1823. https://doi.org/10.1038/s41467-020-15580-7

Milliner, C., Bürgmann, R., Inbal, A., Wang, T., & Liang, C. (2020). Resolving the Kinematics and Moment Release of Early Afterslip Within the First Hours Following the 2016 Mw 7.1 Kumamoto Earthquake: Implications for the Shallow Slip Deficit and Frictional Behavior of Aseismic Creep. *Journal of Geophysical Research: Solid Earth*, *125*(9), 1–18. https://doi.org/10.1029/2019JB018928

Moreno, M. S., Bolte, J., Klotz, J., & Melnick, D. (2009). Impact of megathrust geometry on inversion of coseismic slip from geodetic data: Application to the 1960 Chile earthquake. *Geophysical Research Letters*, *36*(16), 1–5. https://doi.org/10.1029/2009GL039276

Okada, Y. (1985). Surface deformation due to shear and tensile faults in a half-space. *Bulletin of the Seismological Society of America*, *75*(4), 1135–1154. https://doi.org/10.1016/0148-9062(86)90674-1

Ong, S. Q. M., Barbot, S., & Hubbard, J. (2019). Physics-Based Scenario of Earthquake Cycles on the Ventura Thrust System, California: The Effect of Variable Friction and Fault Geometry. *Pure and Applied Geophysics*. https://doi.org/10.1007/s00024-019-02111-9

Otsubo, M., Hardebeck, J. L., Miyakawa, A., Yamaguchi, A., & Kimura, G. (2020). Localized fluid discharge by tensile cracking during the post-seismic period in subduction zones. *Scientific Reports*, *10*(1), 1–8. https://doi.org/10.1038/s41598-020-68418-z

Page, M., Mai, P. M., & Schorlemmer, D. (2011). Testing Earthquake Source Inversion Methodologies. *Eos, Transactions American Geophysical Union*, *92*(9), 75–75. https://doi.org/10.1029/2011EO090007

Perfettini, H., & Avouac, J.-P. (2004). Postseismic relaxation driven by brittle creep: A possible mechanism to reconcile geodetic measurements and the decay rate of aftershocks, application to the Chi-Chi earthquake, Taiwan. *Journal of Geophysical Research: Solid Earth*, *109*(B2), 1–15. https://doi.org/10.1029/2003JB002488

Poblet, J., & McClay, K. (1996). Geometry and kinematics of single-layer detachment folds. *American Association of Petroleum Geologists Bulletin*, *80*(7), 1085–1109. https://doi.org/10.1306/64ed8ca0-1724-11d7-8645000102c1865d

Qiu, Q., Hill, E. M., Barbot, S., Hubbard, J., Feng, W., Lindsey, E. O., et al. (2016). The mechanism of partial rupture of a locked megathrust: The role of fault morphology. *Geology*, *44*(10), 875–878. https://doi.org/10.1130/G38178.1

Ragon, T., Sladen, A., Bletery, Q., Vergnolle, M., Cavalié, O., Avallone, A., et al. (2019). Joint Inversion of Coseismic and Early Postseismic Slip to Optimize the Information Content in Geodetic Data: Application to the 2009 M w 6.3 L'Aquila Earthquake, Central Italy. *Journal of Geophysical Research: Solid Earth*, *124*(10), 10522–10543. https://doi.org/10.1029/2018JB017053

Ramberg, H. (1963). Evolution of Drag Folds. *Geological Magazine*, *100*(2), 97–106. https://doi.org/10.1017/S0016756800055321

Ramberg, H. (1970). Folding of laterally compressed multilayers in the field of gravity, I. *Physics of the Earth and Planetary Interiors*, *2*(4), 203–232. https://doi.org/10.1016/0031-9201(70)90010-5

Ramberg, I. B., & Johnson, A. M. (1976). A theory of concentric, kink and sinusoidal folding and of monoclinal flexuring of compressible, elastic multilayers. *Tectonophysics*. https://doi.org/10.1016/0040-1951(76)90066-4

Reid, H. F. (1911). The elastic-rebound theory of earthquakes. *Univ. Calif. Publ.. Bull. Dept. Geol.*, *6*(19), 413–444.

Rice, J. R., & Ruina, A. L. (1983). Stability of steady frictional slipping. *Journal of Applied Mechanics, Transactions ASME*, *50*(2), 343–349. https://doi.org/10.1115/1.3167042

Rice, James R. (1993). Spatio-temporal complexity of slip on a fault. *Journal of Geophysical Research*, *98*(B6), 9885. https://doi.org/10.1029/93JB00191

Romanet, P. (2020). Curvature, a mechanical link between the geometrical complexities of a fault: application to bends, kinks and rough faults. *Geophysical Journal International*.

Rubin, A. M., & Ampuero, J. P. (2005). Earthquake nucleation on (aging) rate and state faults. *Journal of Geophysical Research: Solid Earth*, *110*(11), 1–24. https://doi.org/10.1029/2005JB003686

Ruina, A. (1983). Slip instability and state variable friction laws. *Journal of Geophysical Research: Solid Earth*, *88*(B12), 10359–10370. https://doi.org/10.1029/JB088iB12p10359

Saillard, M., Audin, L., Rousset, B., Avouac, J. P., Chlieh, M., Hall, S. R., et al. (2017). From the seismic cycle to long-term deformation: linking seismic coupling and Quaternary coastal geomorphology along the Andean megathrust. *Tectonics*, *36*(2), 241–256. https://doi.org/10.1002/2016TC004156

Sathiakumar, S., Barbot, S., & Hubbard, J. (2020). Earthquake cycles in fault-bend folds. *Journal of Geophysical Research: Solid Earth*, 1–62. https://doi.org/10.1029/2019jb018557

Savage, J. C. (1983). A dislocation model of strain accumulation and release at a subduction zone. *Journal of Geophysical Research*, *88*(B6), 4984. https://doi.org/10.1029/JB088iB06p04984

Scholz, C. H. (1998). Earthquakes and friction laws. *Nature*, *391*, 37–42. https://doi.org/10.1038/34097

Segall, P. (2010). *Earthquake and Volcano Deformation. Van Nostrand's Scientific Encyclopedia*. Princeton: Princeton University Press. https://doi.org/10.1515/9781400833856

Shaw, J. H., Bilotti, F., & Brennan, P. A. (1999). Patterns of imbricate thrusting. *Bulletin of the Geological Society of America*, *111*(8), 1140–1154. https://doi.org/10.1130/0016-7606(1999)111<1140:POIT>2.3.CO;2

Sibson, R. H. (2019). Arterial faults and their role in mineralizing systems. *Geoscience Frontiers*, (xxxx), 1–9. https://doi.org/10.1016/j.gsf.2019.01.007

Simons, M., & Rosen, P. A. (2007). Interferometric Synthetic Aperture Radar Geodesy. *Treatise on Geophysics*, *3*, 391–446. https://doi.org/10.1016/B978-044452748-6.00059-6

Singh, S. J., & Rani, S. (1993). Crustal deformation associated with two-dimensional thrust faulting. *Journal of Physics of the Earth*, *41*(2), 87–101. https://doi.org/10.4294/jpe1952.41.87

Souter, B. J., & Hager, B. H. (1997). Fault propagation fold growth during the 1994 Northridge, California, earthquake? *Journal of Geophysical Research-Solid Earth*, *102*(B6), 11931–11942. https://doi.org/10.1029/97jb00209

Suppe, J. (1983). Geometry and kinematics of fault-bend folding. *American Journal of Science*, *283*(7), 684–721. https://doi.org/10.2475/ajs.283.7.684

Suppe, John, Connors, C. D., & Zhang, Y. (2005). Shear fault-bend folding. *AAPG Memoir*, (82), 303–323. https://doi.org/10.1306/m82813c17

Tal, Y., Hager, B. H., & Ampuero, J. P. (2018). The Effects of Fault Roughness on the Earthquake Nucleation Process. *Journal of Geophysical Research: Solid Earth*, *123*(1), 437–456. https://doi.org/10.1002/2017JB014746

Vergne, J., Cattin, R., & Avouac, J. P. (2001). On the use of dislocations to model interseismic strain and stress build-up at intracontinental thrust faults. *Geophysical Journal International*, *147*(1), 155–162. https://doi.org/10.1046/j.1365-246X.2001.00524.x

Walker, R. T., Khatib, M. M., Bahroudi, A., Rodés, A., Schnabel, C., Fattahi, M., et al. (2015). Co-seismic, geomorphic, and geologic fold growth associated with the 1978 Tabas-e-Golshan earthquake fault in eastern Iran. *Geomorphology*, *237*, 98–118. https://doi.org/10.1016/j.geomorph.2013.02.016

Yabuki, T., & Matsu'ura, M. (1992). Geodetic data inversion using a Bayesian information criterion for spatial distribution of fault slip. *Geophysical Journal International*, *109*(2), 363–375. https://doi.org/https://doi.org/10.1111/j.1365-246X.1992.tb00102.x

Yue, L. F., Suppe, J., & Hung, J. H. (2005). Structural geology of a classic thrust belt earthquake: The 1999 Chi-Chi earthquake Taiwan (Mw= 7.6). *Journal of Structural Geology*, *27*(11), 2058–2083. https://doi.org/10.1016/j.jsg.2005.05.020

van Zelst, I., Wollherr, S., Gabriel, A. A., Madden, E. H., & van Dinther, Y. (2019). Modeling Megathrust Earthquakes Across Scales: One-way Coupling From Geodynamics and Seismic Cycles to Dynamic Rupture. *Journal of Geophysical Research: Solid Earth*, *124*(11), 11414–11446. https://doi.org/10.1029/2019JB017539

Zhou, Y., Walker, R. T., Hollingsworth, J., Talebian, M., Song, X., & Parsons, B. (2016). Coseismic and postseismic displacements from the 1978 Mw7.3 Tabas-e-Golshan earthquake in eastern Iran. *Earth and Planetary Science Letters*, *452*, 185–196. https://doi.org/10.1016/j.epsl.2016.07.038

Zhou, Y., Thomas, M. Y., Parsons, B., & Walker, R. T. (2018). Time-dependent postseismic slip following the 1978 Mw7.3 Tabas-e-Golshan, Iran earthquake revealed by over 20 years of ESA InSAR observations. *Earth and Planetary Science Letters*, *483*, 64–75. https://doi.org/10.1016/j.epsl.2017.12.005

Van Zwieten, G. J., Hanssen, R. F., & Gutiérrez, M. a. (2013). Overview of a range of solution methods for elastic dislocation problems in geophysics. *Journal of Geophysical Research: Solid Earth*, *118*(4), 1721–1732. https://doi.org/10.1029/2012JB009278